

# Transition of the Hurricane Boundary Layer during the Landfall of Hurricane Irene (2011)

A. ADDISON ALFORD

*School of Meteorology, University of Oklahoma, Norman, Oklahoma*

JUN A. ZHANG

*NOAA/Atlantic Oceanographic and Meteorological Labs/Hurricane Research Division, and Cooperative Institute for Marine and Atmospheric Studies, University of Miami, Miami, Florida*

MICHAEL I. BIGGERSTAFF

*School of Meteorology, and Advanced Radar Research Center, and Cooperative Institute for Mesoscale Meteorological Studies, University of Oklahoma, Norman, Oklahoma*

PETER DODGE AND FRANK D. MARKS

*NOAA/Atlantic Oceanographic and Meteorological Labs/Hurricane Research Division, Miami, Florida*

DAVID J. BODINE

*Advanced Radar Research Center, University of Oklahoma, Norman, Oklahoma*

(Manuscript received 16 October 2019, in final form 27 February 2020)


## ABSTRACT

The hurricane boundary layer (HBL) has been observed in great detail through aircraft investigations of tropical cyclones over the open ocean, but the coastal transition of the HBL has been less frequently observed. During the landfall of Hurricane Irene (2011), research and operational aircraft over water sampled the open-ocean HBL simultaneously with ground-based research and operational Doppler radars onshore. The location of the radars afforded 13 h of dual-Doppler analysis over the coastal region. Thus, the HBL from the coastal waterways, through the coastal transition, and onshore was observed in great detail for the first time. Three regimes of HBL structure were found. The outer bands were characterized by temporal perturbations of the HBL structure with attendant low-level wind maxima in the vicinity of rainbands. The inner core, in contrast, did not produce such perturbations, but did see a reduction of the height of the maximum wind and a more jet-like HBL wind profile. In the eyewall, a tangential wind maximum was observed within the HBL over water as in past studies and above the HBL onshore. However, the transition of the tangential wind maximum through the coastal transition showed that the maximum continued to reside in the HBL through 5 km inland, which has not been observed previously. It is shown that the adjustment of the HBL to the coastal surface roughness discontinuity does not immediately mix out the residual high-momentum jet aloft. Thus, communities closest to the coast are likely to experience the strongest winds onshore prior to the complete adjustment of the HBL.

## 1. Introduction

Understanding the distribution of winds, intensity change, and tropical cyclone (TC) structure requires comprehensive knowledge of the storm's atmospheric boundary layer [hereafter referred to as the hurricane boundary layer (HBL); e.g., [Montgomery et al. 2014](#)]. The structure of the HBL can influence the vertical

---

 Denotes content that is immediately available upon publication as open access.

---

*Corresponding author:* Dr. Michael I. Biggerstaff, [drdoppler@ou.edu](mailto:drdoppler@ou.edu)

DOI: 10.1175/JAS-D-19-0290.1

© 2020 American Meteorological Society. For information regarding reuse of this content and general copyright information, consult the [AMS Copyright Policy](#) ([www.ametsoc.org/PUBSReuseLicenses](http://www.ametsoc.org/PUBSReuseLicenses)).

distribution of momentum through turbulent fluxes, which in turn can influence the horizontal distribution of the maximum wind experienced at any one location, particularly during landfall (Wurman and Winslow 1998; Alford et al. 2019). Due to the increase in aerodynamic surface roughness over land versus that over the open ocean, sustained wind speeds are expected to decrease while the dynamic boundary layer is expected to increase in depth (Elliott 1958; Garratt 1990; Tang and Tan 2006; Hirth et al. 2012; Williams 2019).

Observations of the mean HBL structure over the open ocean are generally plentiful (Zhang et al. 2011; Ren et al. 2019). High-vertical-resolution (10–20 m) dropsonde (Hock and Franklin 1999) observations have been collected by several airborne platforms including the National Oceanic and Atmospheric Administration's (NOAA's) WP-3D Orion and G-IV jet (Aberson et al. 2006) operated by the NOAA Aircraft Operations Center, the C-130 Hurricane Hunter aircraft operated by the U.S. Air Force (USAF; e.g., Franklin et al. 2003), the HIAPER aircraft operated by National Science Foundation (NSF; UCAR/NCAR 2005), and the DC-8 and Global Hawk operated by the National Aeronautics and Space Administration (NASA; Naftel 2009). Such observations have documented the vertical thermodynamic and kinematic structure of TCs over large mesoscale regions across the entire cyclone and surrounding environment. The mean structure of the HBL has been elucidated through individual and composite dropsonde observations over hurricanes of varying strengths and varying degrees of symmetry (e.g., Franklin et al. 2003; Kepert 2006; Zhang et al. 2011, 2013). In general, it has been found that the top of the dynamic HBL (i.e., the level at which the hurricane radial inflow is 10% of its peak value) decreases with height with decreasing radial distance from the center of circulation (Zhang et al. 2011; Giammanco et al. 2013). Wind profiles often exhibit a distinct peak (or jet) within the dynamic HBL, usually near the inner core of the tropical cyclone (Giammanco et al. 2013). Numerical modeling studies have focused on replicating the HBL as observed in nature, often finding that the representation of the HBL is highly sensitive to model diffusion and HBL parameterization schemes (e.g., Tang and Tan 2006; Bryan and Rotunno 2009; Nolan et al. 2009b,a).

In contrast to the open-water HBL, the structure of the HBL across the land–water interface across the coast is not as well documented. Observations over the land surface are limited by aircraft flight safety concerns while the sparse nature of profiling systems over land limit where vertical profiles of the boundary layer may be retrieved. Nonetheless, a few observational studies have been performed (Morrison et al. 2005; Lorsolo et al. 2008; Giammanco et al. 2013; Hirth et al. 2012; Ming et al. 2014).

Hirth et al. (2012) found that an internal boundary layer (IBL; cf. Garratt 1990) formed across the land–ocean interface during the landfall of Hurricane Frances (2004). The IBL resulted from the surface roughness discontinuity across the coastal transition. In general terms, the IBL forms due to a discontinuity in, for example, aerodynamic surface roughness (e.g., an ocean–land interface) as flow passes across the discontinuity (e.g., Garratt 1990; Savelyev and Taylor 2005). All else being equal downwind of the discontinuity, the boundary layer adjusts to the new surface roughness characteristics such that the IBL grows until it represents the complete depth of the fully adjusted boundary layer (see Hirth et al. 2012, their Fig. 6). In Hirth et al. (2012), the complexity of the coastal environment and the attendant adjustment of the HBL were examined. Across the coastal interface, the modeled empirical growth of the IBL was observed to be less than expected. Due to inhomogeneities in surface roughness and the added complexity of coastal islands, the structure of the growing boundary layer was far from homogeneous in their analyses. In addition, significant backing of the low-level (400–500 m) winds was observed in their analyses, with changes in wind direction of 15°–20° immediately inland.

Using velocity–azimuth display (VAD) profiles, Giammanco et al. (2013) demonstrated that the evolution of onshore and offshore flow denoted by normalized boundary layer mean wind profiles were relatively similar. Specifically, the reduction in the boundary layer height with decreasing storm-center-relative radial distance was found for both onshore and offshore regimes. Jet-like features were observed in profiles in both regimes as well, largely tied to regions near the radius of maximum wind (RMW). However, significant differences were found in onshore and offshore wind profile structures for the same normalized radial distances. Surface roughness and upwind terrain characteristics were found to change the vertical structure of the boundary layer significantly. The authors also made mention of jet-like features in outer rainbands, similarly found in Knupp et al. (2006). Neglecting storm-relative space, Krupar et al. (2016) used VAD profiles to estimate the surface wind speed in 17 hurricane landfalls. It was found that WSR-88D site-specific constructions of linear regression equations yielded the most accurate surface wind estimates. However, the authors acknowledged that VAD retrievals are limited in assessing HBL characteristics across large spatial regions and emphasized the need for spatially contiguous observations from, for example, dual-Doppler analyses across the coastal region.

Ming et al. (2014) documented fluctuations in HBL structure with the passage of outer rainbands in

Typhoon Morakot (2009). Downdrafts associated with rainbands tended to reduce the height of the tangential wind maximum. Contrary to most studies, Ming et al. found that the tangential wind maximum in the outer rainbands was above the height of the dynamic HBL and suggested the observation could be the direct result of landfall processes. However, no study has been able to address the change of the height of the tangential wind maximum while observing both onshore and over-water boundary layer structure and the transition between the two. If the observation of the tangential wind maximum above the boundary layer is generally applicable to TC landfalls, then the landfall HBL transition is likely important in the vertical momentum structure observed over land. In particular, the projection of momentum aloft via turbulence on a variety of spatial scales has been shown to be fundamental in the magnitude of gusts observed at the surface (Morrison et al. 2005; Lorsolo et al. 2008; Kosiba and Wurman 2014). Furthermore, individual convective processes such as rainbands are also likely fundamental to the observed vertical distribution of momentum. However, a comparison of the HBL in rainbands to that of the inner core and eyewall has not been examined within an individual storm.

In this study, the transition of the HBL, specifically the structure of the sustained wind, during the landfall of Irene (2011) will be documented quantitatively using over-ocean dropsonde observations, land-based VAD retrievals from ground-based Doppler radars, and dual-Doppler wind retrievals. The study is unique in that the observations over land and water were collected within the same time period. Flow regimes in the outer bands, the inner core, and eyewall can also be directly compared. Moreover, one set of VAD winds is from a frequency-agile Doppler radar with a temporal resolution of approximately 30 s and can be used to extend the information extracted from dual-Doppler analyses (available every 10 min). Additionally, the dual-Doppler domain includes portions of the coastal interface. Hence, for the first time, the mean HBL can be examined near simultaneously from over water, through the coastal transition, and inland. Specifically, the transition of the tangential wind maximum will be shown as the HBL changes in response to the coastal surface roughness discontinuity. The coastal transition, in particular, is herein documented with high temporal and spatial resolution across a limited domain within  $\pm 10$  km from the land–water interface and extended through dropsonde and VAD analyses.

## 2. Data and methods

Noted in Avila and Cangialosi (2012), Hurricane Irene (2011) began as a tropical wave originating off the

coast of Africa on 15 August and became a tropical storm on 21 August east of Dominica. At its most intense period, Irene struck the Bahamas as a category 3 hurricane ( $50\text{--}58\text{ m s}^{-1}$ ) before moving north and beginning to weaken. On 27 August, Irene made landfall near Cape Lookout, North Carolina, as a category 1 storm (estimated  $38.6\text{ m s}^{-1}$  maximum sustained 1-min wind at 10-m altitude). In addition to flooding and wind damage experienced in North Carolina, Irene produced tremendous inland flooding in parts of New England before making its extratropical transition at higher latitudes.

During its landfall in North Carolina, simultaneous observations by the NOAA aircraft and ground-based mobile and stationary radars afford the retrieval of boundary layer structure over the open ocean, in coastal waterways, and onshore. At the time of simultaneous observations prior to and during landfall, Irene was considered a category 1 hurricane with a maximum sustained wind of  $\sim 38\text{ m s}^{-1}$ . The observational period (0000 to 1300 UTC) encompasses the outer bands, inner core (generally the annulus bounded by the RMW wind to a radial approximately 3 times that of the RMW), and eyewall (cf. Houze 2010).

### a. Dropsondes

GPS dropwindsondes (here referred to as “dropsondes”) are commonly released by the NOAA P-3 to characterize vertical structure of temperature, relative humidity, pressure, and horizontal and vertical wind speeds and directions in hurricanes (e.g., Franklin et al. 2003; Halverson et al. 2006; Stern et al. 2016; Rogers et al. 2017). The details of a dropsonde and its measurement errors can be found in Hock and Franklin (1999) and Zhang et al. (2011, their section 2b). Here, the dropsonde kinematic data are especially useful for characterizing the vertical structure of the HBL winds and are exclusively utilized for consistency with other datasets described below. In addition, we interpret the depth of the boundary layer height according to the dynamic definition recommended in Zhang et al. (2011).

During Hurricane Irene, the NOAA P-3, the NOAA G-IV (Aberson and Franklin 1999), and Air Force Reconnaissance aircraft conducted a series of flights near landfall that will be the focus of this study (see Figs. 1a,c). Dropsondes used in this study were limited to 27 August 2011 to be representative of the environment over water in close proximity to available land-based instrumentation. All dropsondes were processed using the National Center for Atmospheric Research’s (NCAR’s) Atmospheric Sounding Processing Environment (ASPEN) software as described in Zhang et al. (2013). The fall speed of a typical dropsonde is  $12\text{--}14\text{ m s}^{-1}$  and the sampling rate is 2 Hz, yielding 5–7-m vertical sampling. The 2-Hz sample

## HURRICANE IRENE

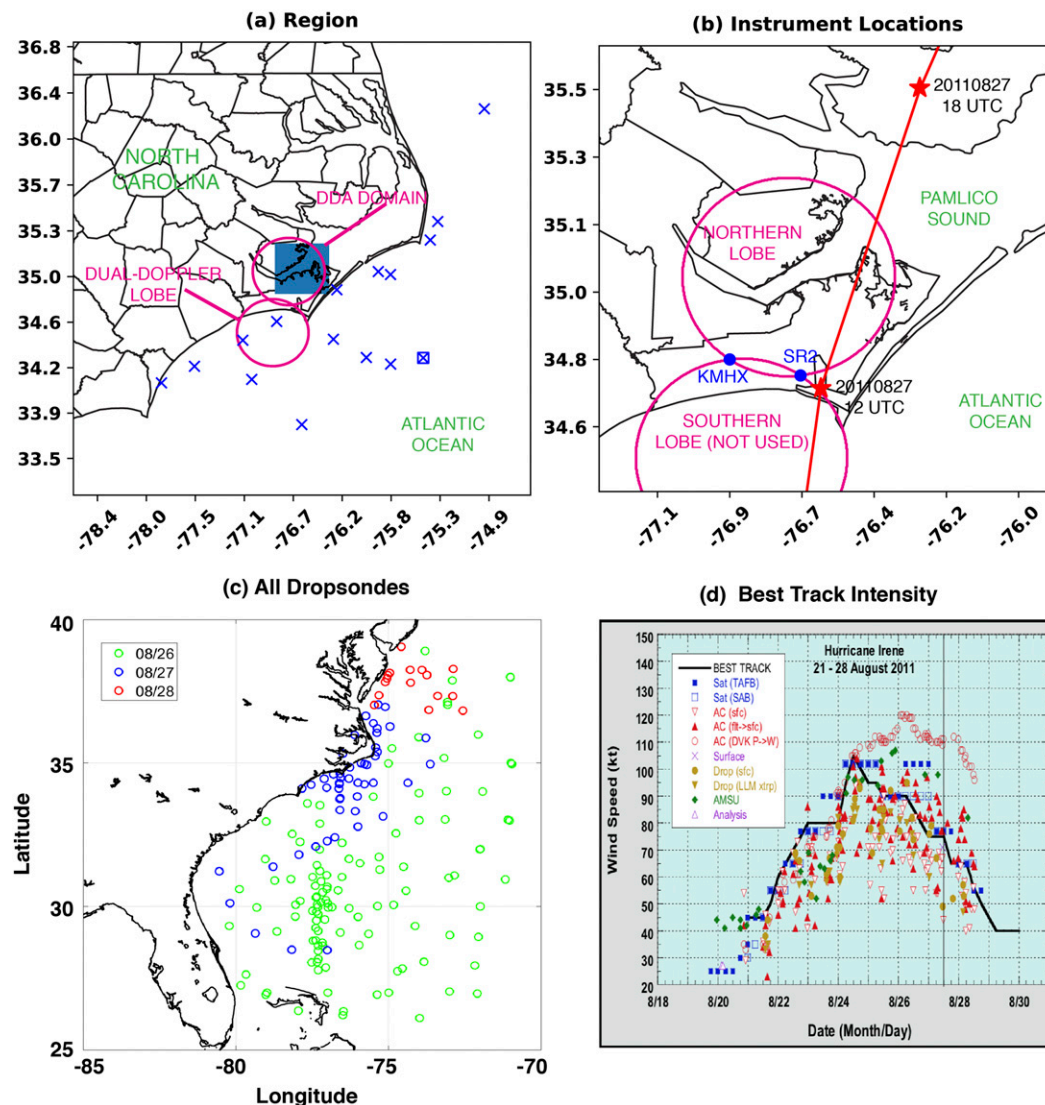


FIG. 1. Details of the observation, instrumentation, and dual-Doppler domain locations. (a) A large view of the region over which observations were collected. The blue  $\times$  symbols indicate locations of dropsondes released by the NOAA P-3 within 100 km of the coast that were used in this study. The blue cross enclosed by a box denotes the single dropsonde collected over deep, nonshoaling water. (b) A detailed view of the dual-Doppler lobes (magenta lines) and the locations of KMHX and SR2 (blue circles). RaXPoI was collocated with SR2. The red line indicates the best track locations of Irene with synoptic dates and times indicated by the red stars. (c) The locations of dropsondes released by the NOAA P-3, G-IV, and Air Force C-130 are shown colored by date. (d) The National Hurricane Center best track intensity in time (figure courtesy of [Avila and Cangialosi 2012](#)).

was filtered over 5-s intervals in ASPEN, yielding approximately 10-m resolution.

#### b. SMART radar and Morehead WSR-88D

The University of Oklahoma (OU) Shared Mobile Atmospheric Research and Teaching (SMART) radar 2 (SR2; [Biggerstaff et al. 2005, 2017](#)) was deployed to Michael J. Smith Airfield near Beaufort,

North Carolina, prior to Hurricane Irene's landfall. SR2 (located at  $34.7331^\circ$ ,  $-76.6619^\circ$ ) operated continuously for approximately 15 h between 2100 UTC 26 August and 1215 UTC 27 August 2011. While SR2 collected data to achieve a variety of science objectives, SR2 scan volumes that were appropriate for performing dual-Doppler analysis with the nearby WSR-88D ([Crum and Alberty 1993](#)) in Morehead City, North Carolina



(KMHX; located at  $34.7760^\circ$ ,  $-76.8762^\circ$ ), were collected every 10 min.

Level II data for KMHX were retrieved from the National Centers for Environmental Information (available at <https://www.ncdc.noaa.gov>). Dual-Doppler analyses were conducted between 0000 and 1215 UTC 27 August. While SR2 collected data beginning at 2100 UTC 26 August, KMHX data between 1800 and 2359 UTC 26 August were unavailable, and hence no dual-Doppler analyses were performed. The radial velocities from both radars were objectively dealiased using the region-based dealiasing method available in the Python-ARM Radar Toolkit (Py-ART; [Helmus and Collis 2016](#)). SR2 was operated in staggered pulse repetition time (PRT) mode ([Torres et al. 2004](#)), which extends the unambiguous Doppler velocity interval. Errors associated with the staggered PRT method were corrected after the radial velocity data were dealiased.

The radar reflectivity ( $Z_H$ ) and Doppler velocity ( $V_R$ ) data were interpolated to a Cartesian grid using a natural neighbor interpolation ([Sibson 1981](#)) method documented in [Betten et al. \(2018\)](#). The Cartesian grid had an origin set to the location of KMHX, with minimum  $x$ ,  $y$ , and  $z$  distances of 5, 5, and 0.2 km and maximum  $x$ ,  $y$ , and  $z$  distances of 50, 50, and 10.2 km, respectively. The 20-km baseline between the radars provided high spatial resolution over the analysis domain, and horizontal and vertical spacing were set to 250 and 200 m, respectively. Because the southern dual-Doppler domain was largely affected by ground-clutter from Morehead City, the northern dual-Doppler lobe, which extended over a saltwater inlet and open fields, were exclusively used here ([Fig. 1b](#)).

The interpolated data were passed into a three-dimensional variational (3DVAR) dual-Doppler analysis technique documented by [Potvin et al. \(2012\)](#). This technique is designed to heavily weigh the observed radial velocity fields when storm-topping echoes are not available (i.e., when the column total mass continuity is under sampled). As the dual-Doppler domain is relegated to below the storm tops at times, this technique is heavily favored for the retrieval of the horizontal winds, rather than traditional, iterative techniques that require better sampling of a column's total divergence profile.

In addition to dual-Doppler analysis, range–height indicator scans (RHIs) were collected by SR2. However, the azimuths over which the RHIs were taken varied at the discretion of the radar operator. To provide a more consistent set of vertical cross sections, RHIs were developed from the volumetric scans over a  $15^\circ$  azimuthal sector every  $3^\circ$ , yielding five total RHIs per volume. The radial velocity field was dealiased manually in all cases using Solo3 ([Oye et al. 1995](#)).

### c. RaXPOL data

The Rapid X-Band Dual-Polarimetric Radar (RaXPOL; [Pazmany et al. 2013](#); [Pilkey et al. 2013](#)) was deployed nearly collocated with SR2 in Beaufort, North Carolina. Using a frequency-agile transmitter, RaXPOL collects data at a maximum azimuthal antenna rotation rate of  $180^\circ \text{ s}^{-1}$ . During the landfall of Irene, RaXPOL operated at  $120^\circ \text{ s}^{-1}$ , yielding one elevation scan every 3 s (excluding time to transition the antenna to the next elevation). RaXPOL primarily operated between 0000 and 0500 UTC, affording high-temporal-resolution Doppler velocity retrievals of the HBL within 30 km of the radar's location ( $34.7300^\circ$ ,  $-76.6570^\circ$ ) during the landfall of Irene's outer bands. The data were similarly processed through Py-ART's region-based dealiasing scheme. These data were analyzed using a VAD technique described below.

### d. Coastal VADs

The VAD technique described in [Browning and Wexler \(1968\)](#) was used to construct representative profiles of the boundary layer wind structure from Doppler radar. The technique involves using Doppler velocity observations around constant radii circles to retrieve the mean flow at constant heights. The fit of Fourier coefficients to the radial velocity observations assumes that the flow characteristics around a constant radial circle vary at most linearly across the circle.

The vertical resolution of the constructed vertical profiles is dependent on the radial resolution of the radar data. Profiles were constructed for both KMHX and RaXPOL radial velocity observations. KMHX collected data at 250-m radial resolution. Using radial velocity data between 0.15 and 8.0 km from KMHX, VADs with an average resolution of  $\sim 7$  m in the vertical were obtained and a maximum resolution of  $\sim 85$  m. Thus, data were linearly interpolated to 15-m vertical resolution. The temporal resolution was approximately every 5 min for VADs retrieved between 0000 and 1300 UTC 27 August. RaXPOL obtained radial velocity data at much higher temporal and radial resolutions. The vertical resolution varied between 15 and 75 m, so the VAD profiles were linearly interpolated to a resolution of 15 m in the vertical. Radar volumes were obtained approximately every 30 s, yielding high temporal resolution observations of the boundary layer wind profiles. The observation period of RaXPOL was largely confined to 0000 to 0500 UTC, during which time the outer bands of Irene were moving on shore.

## 3. Open-water dropsonde profiles

To facilitate compositing of the HBL vertical profiles within the storm's dynamic framework, observations of

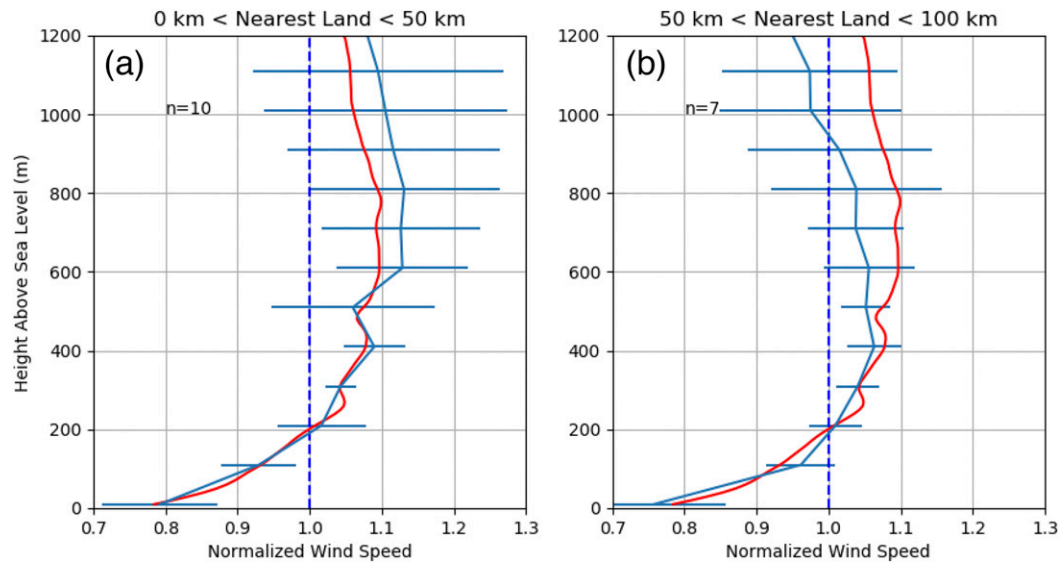


FIG. 2. Normalized dropsonde profiles taken (a) from 0 to 50 km of the nearest point on the coast and (b) from 50 to 100 km of the nearest point on the coast. The dashed blue line indicates a normalized wind speed of 1.0. The cyan line shows the mean of  $n$  profiles taken for each distance subset on 27 Aug 2011. The red line indicates the mean of all dropsondes profiles regardless of date. Error bars are  $\pm 1$  standard deviation.

the RMW based on stepped frequency microwave radiometer (SFMR; e.g., Uhlhorn and Black 2003) data were used to normalize the radial distance from the center of circulation ( $r$ ) relative to the RMW using (1):

$$r^* = \frac{r}{\text{RMW}}. \quad (1)$$

Total wind speed dropsonde observations from 27 August 2011 prior to and during Hurricane Irene's landfall were composited for the lowest 1200-m altitude by the normalized radius  $r^*$ . Dropsondes with drop points  $0.8 < r^* < 3$  and distances between 0 and 100 km from the nearest point on the coast were retained for this study. This method yielded 10 dropsondes taken within 50 km of the nearest coastline (near coast) and 7 dropsondes between 50 and 100 km of the coastline (far coast; Fig. 1a). The wind speeds are also normalized by the mean 10–500-m wind speed observed by each dropsonde unless otherwise noted.

Although a relatively small sample for each set of coast-relative distances, Fig. 2 shows the mean normalized profiles for the near and far coast dropsondes. All profiles were taken within 100 km of the coastline and over the North American continental shelf. One dropsonde (highlighted in Fig. 1) was dropped just beyond the continental shelf, but is retained as it was very near the gradient in bathymetry. Hence, we take the dropsonde profiles as representative of shoaling wave conditions (Powell et al. 2003), where drag coefficients are

increased relative to deep water (e.g., beyond the continental shelf). Each profile shows normalized wind speed maxima well above the surface. In addition, both regions exhibit mean 10-m normalized winds that are less than 0.8 of the 0–500-m mean flow, similar to past studies (e.g., Kepert 2001). The composite profiles yield several results of note. First, the normalized wind speeds in the lowest 100 m of both near and far coast profiles are significantly more variable than other winds below 500 m, with standard deviations on the order of 0.10–0.15 of the normalized mean wind speed. A similar increase in the variability of the normalized profile was recorded in Giammanco et al. (2013). Second, while the magnitudes of the mean 10 m wind speed normalized by the 0–500-m mean are similar for the near coast (0.79; Fig. 2a) and far coast (0.76; Fig. 2b), the structure of the normalized profiles differ strongly aloft. The near coast profiles exhibit their maximum values around 600–800-m altitude while the far coast wind speeds are maximized at approximately 400 m. The “jet” structure exhibited by both profiles is consistent with previous observations of the HBL observed well over water (e.g., Zhang et al. 2011; Giammanco et al. 2013).

The robustness of the limited observations taken on 27 August was compared using all the dropsondes in Hurricane Irene between 26 and 28 August 2011 and for  $0.8 < r^* < 3.0$  (shown as red lines in Fig. 2). However, to generate a larger sample, dropsondes were not delineated according to their coast-relative distance (i.e., dropsondes over the open ocean, well away from the

coast were retained). In total, 42 profiles were retained for comparison to the near and far coast profiles (see red lines in Fig. 2; referred to as the all-profile mean). The profile structure below 400 m delineated by coast-relative distance represented the all-profile mean well. Specifically, the normalized wind speeds at 10 m for the near and far coast profiles were quantitatively similar to the all-profile mean (differences of  $\sim 0.02\text{--}0.03$ ). In addition, the 10–400-m layer for both near coast and far coast profiles are quantitatively representative of all profiles (differences generally less than 0.05). The height of the maximum normalized wind for all dropsondes was 600–800 m, which matched the near coast profile well. In addition, normalized differences of approximately 0.03–0.05 above a height of 600 m exist for near coast profiles, suggesting the entirety of the near coast profile was generally representative of the dataset. However, some differences aloft were noted in the far coast profiles. The far coast profile appeared to suggest a height of the maximum normalized wind to be near 400 m. It is unclear if the differences between all profiles and the far coast profile were due to sampling differences or the smaller number of dropsondes (seven in total). We hypothesize the differences in sample space (particularly sondes dropped at varying  $r^*$ ) to be a more plausible reason for differences in the profiles, rather than the sample size itself.

The observed dropsonde wind profiles can be decomposed into tangential and radial wind components by projecting the wind direction into a storm-center-relative framework using the method of Willoughby and Chelmow (1982). Uncertainty in the exact center of circulation can affect the estimation of the radial wind more strongly than the tangential wind. Nevertheless, the approach has been used in previous studies (e.g., Giammanco et al. 2013) successfully, as it is based upon center-fixes collected by aircraft operations at higher temporal frequency than National Hurricane Center best track estimates. The characteristics of the tangential wind component in the soundings are largely similar to those of the full wind profiles described above (see Figs. 3a,b). In contrast, the radial wind profiles (Figs. 3c,d) exhibit significantly greater variability, likely due to the azimuthal variability in the radial wind. Based on the composite mean, the near coast (0–50 km) profiles (Fig. 3c) suggest that the boundary layer height  $h_{\text{inflow}}$  is approximately 1000 m with the peak tangential (and peak full) wind speed near 800-m altitude (Fig. 2a). This is consistent with past observational studies, which have demonstrated that the maximum tangential wind is often located within the inflow layer as shown here (Vickery et al. 2009; Zhang et al. 2011; Montgomery et al. 2014). To examine the

transition of the boundary layer from the open ocean to the coast, vertical wind profiles were derived from the dual-Doppler analyses.

#### 4. Coastal composite profiles

Since the dual-Doppler domain includes both water and land surfaces, a classification of “land” or “water” was assigned for each dual-Doppler grid point (Fig. 4a) using the Basemap function in Python (available online at <https://matplotlib.org/basemap>). The distance (regardless of wind direction) from the coast was calculated (negative values in Fig. 4b indicate inland and positive indicate over coastal waterways). For each dual-Doppler grid point, a vertical profile normalized by the 0–600-m mean wind (slightly different from the dropsondes in section 3 due to the differing vertical resolution) was constructed. In general, profiles were taken between 10 km inland and 5 km over water ( $-10$  to  $+5$  km) of the coastline. A subset of the dual-Doppler lobe (shown in Fig. 1a) was used in this region. Within the observation period, the mean wind direction across the dual-Doppler domain was between  $\sim 70^\circ$  and  $\sim 110^\circ$  (winds from the east), indicative of onshore flow in the dual-Doppler domain. Since the dual-Doppler subdomain is relatively small, we assume that the water versus land profiles are taken approximately in the same storm-center-relative space. However, differences are readily apparent in the mean winds over land and over water as expected with domain-averaged 0–600-m wind speeds less over land than over water (Figs. 4c,d).

##### a. Over-water HBL structure

To examine the coastal transition of the boundary layer throughout the dual-Doppler observation period, the over-land and over-water profiles were further delineated into subsets representing the distance to the nearest point of coastline. Negative distances indicate profiles over land and positive distances indicate profiles over water. As shown in Fig. 4, the water surfaces used here are confined to coastal waterways that experienced easterly flow throughout the dual-Doppler period. At times depending on the exact wind direction, flow may have undergone transition off of land surfaces into the coastal waterways. Nevertheless, flow was generally in an onshore regime across the domain as a whole.

The result over the full  $\sim 12$ -h period of the dual-Doppler analysis is shown in Fig. 5. The nearshore profiles retrieved by dropsondes in Fig. 2 showed a maximum in normalized wind speed above 600 m. Similarly, the dual-Doppler-derived mean profiles just off the coastline indicate the maximum wind speed was between 400 and 800 m in altitude. Indeed, the general

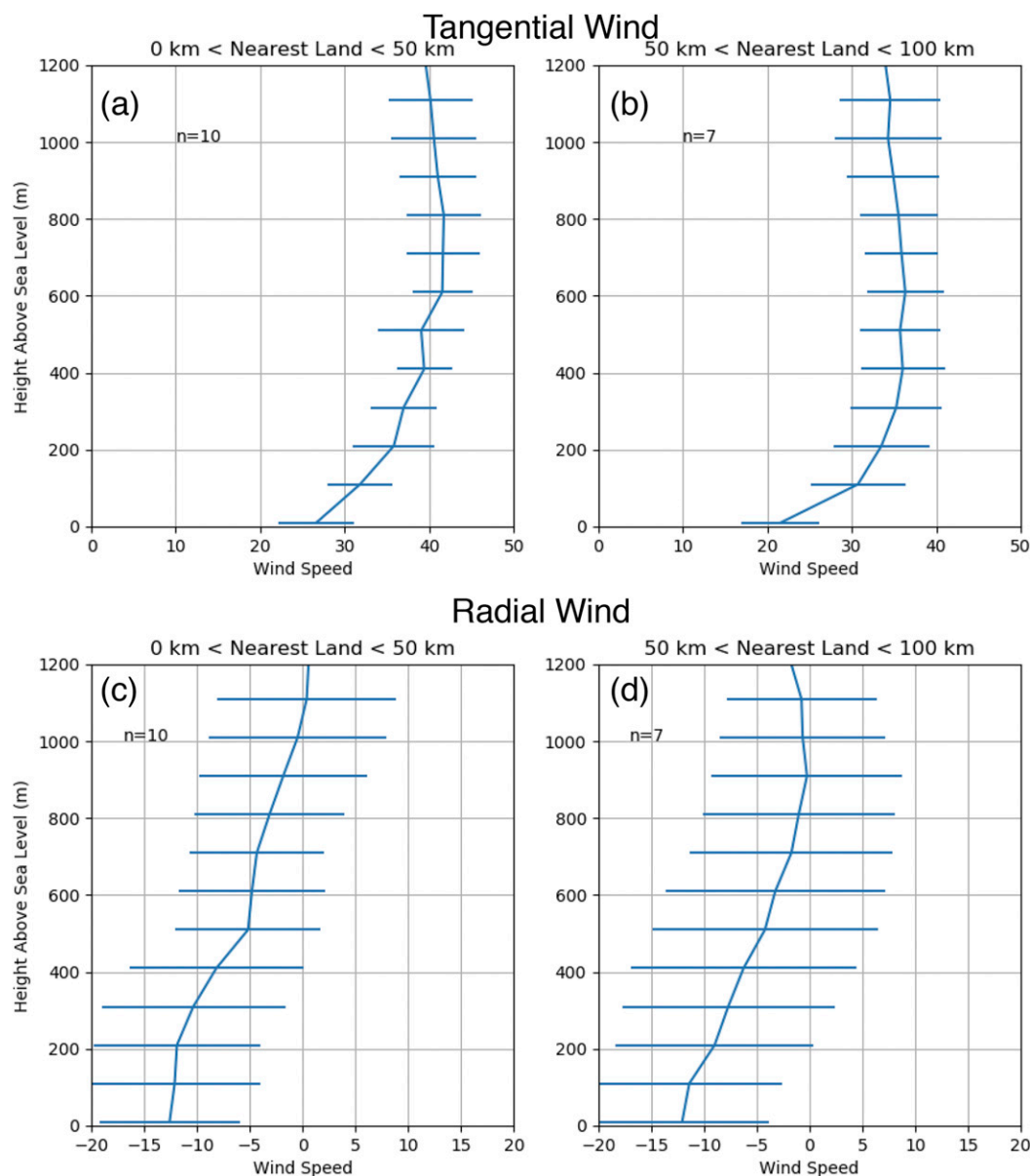


FIG. 3. Dropsonde profiles of nonnormalized (a),(b) tangential and (c),(d) radial wind (relative to the SFMR/best track–derived center of circulation) on 27 Aug 2011. Unlike Fig. 2, the actual wind speed values ( $\text{m s}^{-1}$ ) are shown instead of the normalized wind.

structure of the dual-Doppler normalized winds from 0 to 5 km over water appears similar to the dropsonde-measured boundary layer profiles over water. Specifically, winds between 400 and 800 m generally exceed the boundary layer mean wind by a few percent. Winds between 200 and 400 m are generally near 100% of the boundary layer mean wind or just slightly less than the mean wind speed, similar to dropsonde composites. The profiles in the 0–2.5-km range bins change relative to the 2.5–5.0-km range bins, suggesting the HBL may begin to “feel” the shoreline in the 0–2.5-km bins.

However, it is unclear if this is due to smoothing performed in the interpolation and dual-Doppler analysis, or if the HBL begins adjusting near the shore.

To explore the changes seen in the mean profiles over water nearing the coast, RHIs taken by SR2 are employed. Although RHIs can only resolve the one-dimensional wind directly toward or away from the radar perspective, RHIs of the boundary layer can corroborate the mean structure of the coast-relative boundary layer generated from dual-Doppler analysis. Shown in Figs. 6a and 6b, a single RHI taken at



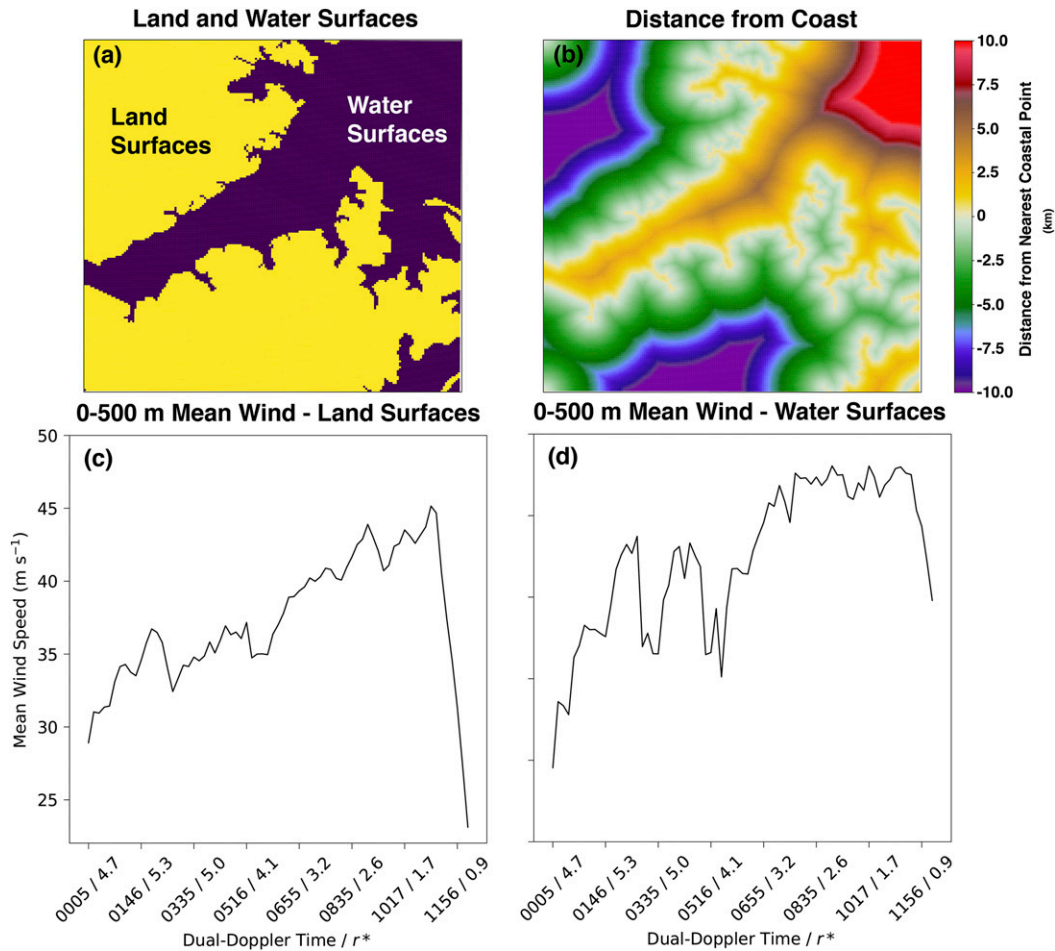


FIG. 4. Details of the dual-Doppler domain land and water surfaces. (a) Land surfaces are shown in yellow and water surfaces are shown in purple. (b) For each grid point in the dual-Doppler domain, the distance (KM) to the nearest coastal point is shown according to the color bar values. Positive values indicate distances of water surfaces from the coast. (c) A time series of the area-average 0–600-m wind speed across the dual-Doppler domain is shown strictly for land surfaces. (d) As in (c), but for water surfaces. In (c) and (d) the  $x$  axis shows the dual-Doppler time and the domain-mean  $r^*$ .

1009 UTC along a rainband exterior of the eyewall (approximately perpendicular to the coast) shows a maximum in  $V_R$  (Doppler velocity) between 500- and 1000-m altitude within 8-km range, where 8 km approximately represents the radar-relative range to the coast (excluding the barrier islands). Beyond 8 km, the  $V_R$  maxima appear to be below 500-m altitude. Additionally,  $V_R$  appears to be relatively constant below 500-m altitude beyond 8 km. Clearly, the structure of  $V_R$  in the plane of the RHI changes abruptly at the coast, rather than transitioning just over water as in the composite dual-Doppler analysis results. Inland from the coast, the maximum  $V_R$  increases in height to between 500 and 1000 m above radar level within approximately 2–3 km of the coastline, similar to what is seen in the dual-Doppler analysis mean. Below 500 m, the

magnitude of  $V_R$  decreases, likely from both the backing of the boundary layer wind and the reduction in the magnitude of the boundary layer wind. Figure 5b corroborates that backing in the plane of the RHI is likely, as the coast-relative mean wind direction in over-water bins in the mean is  $80^\circ$ – $90^\circ$  compared to onshore values of  $70^\circ$ – $80^\circ$  in the lowest 500 m of the atmosphere. This transition occurs rapidly inland of the coastline, suggesting that IBL growth is a function of the discontinuity of surface roughness from water to land surfaces, similar to the results found in Hirth et al. (2012).

An additional RHI (Figs. 6c,d) was examined 10 min (0959 UTC) prior that was farther southwest over a similar portion of the coastal region. Doppler velocities were weaker in this case, as the plane of the RHI was not oriented nearly parallel to the boundary layer wind.

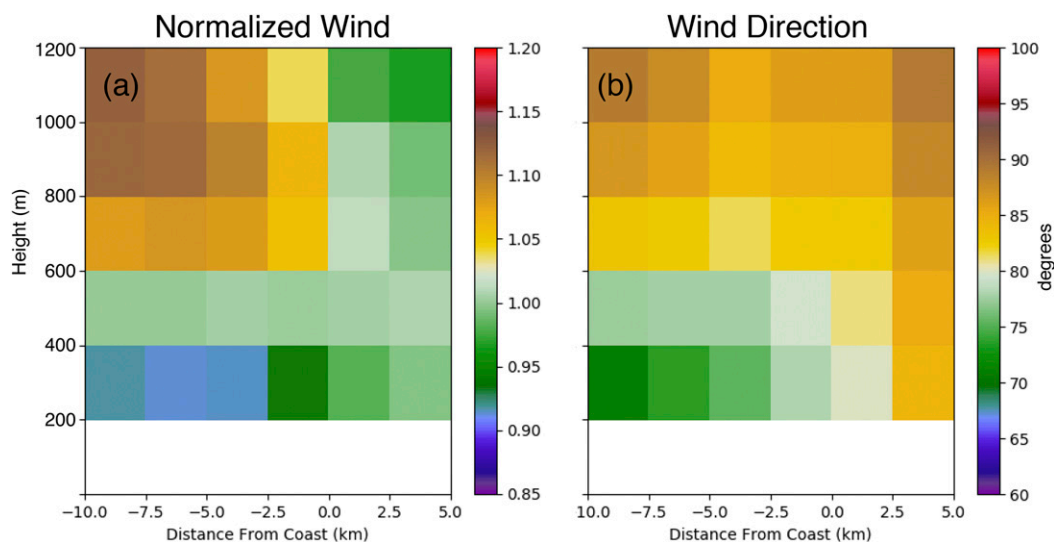


FIG. 5. (a) Coast-relative normalized wind profile averaged in time and distance from the coast for all dual-Doppler profiles between 0000 and 1215 UTC. Positive distances from the coast indicate increasing distance over water surfaces within the dual-Doppler domain. (b) As in (a), but for the wind direction according to the color bar (in degrees from north).

Nevertheless, at approximately 6-km range (corresponding to the coastal region) in Figs. 6c and 6d, the Doppler velocities show a decrease in the  $V_R$  field below 500 m and a similar growth in the depth of the weaker  $V_R$  structure as in the RHI taken at 1009 UTC. There exists an additional perturbation in  $V_R$  at approximately 8.5-km range, which corresponds to the barrier islands shown in the inset in Fig. 6d. As at 1009 UTC, the change in the  $V_R$  field appears to exist coincident with the coastal interface, suggesting that the HBL winds adjust to the underlying surface while the residual  $V_R$  maximum above retains its character.

### b. Inland HBL structure

Onshore, rapid changes in the boundary layer mean winds can be seen beginning in the first range bin inland from the coast (Fig. 5a). An immediate increase in the altitude of the normalized maximum wind can be seen relative to the over-water structure. Winds below 400 m fall below 95% of the boundary layer wind speed. Farther inland, winds fall to about 90% of the mean wind at ranges of  $-10$  to  $-7.5$  km. Over land, the height of the maximum tangential wind (Fig. 7a) appears to shift from heights of 400–800 m over water to 800–1000 m onshore, suggesting that the surface roughness transition at the coast influences the height of the maximum wind.

The actual tangential wind speed profile (Fig. 7a) shows a qualitatively similar structure to the normalized total wind (Fig. 5a), but the actual radial wind speed profile (Fig. 7b) shows the most significant changes

relative to the normalized wind. Rather than using a normalized wind value, which is more heavily affected by values between  $-1$  and  $0 \text{ ms}^{-1}$  (division by a small number), the full radial wind is shown to demonstrate the rapid transition in boundary layer structure across the coast (Fig. 7). Between 2.5 and 5 km over water, the maximum radial inflow in the mean is between 200- and 400-m altitude and changes little toward shore, but increases in magnitude over land. As expected, the radial wind onshore should increase for the same total wind speed, as the degree of imbalance between the Coriolis, centrifugal, pressure gradient, and frictional forces is disrupted relative to over the open ocean.

The height of the mean boundary layer (defined by the height at which the radial inflow is 10% of its peak value; Zhang et al. 2011) appears to be above the height of the maximum tangential wind for over-water profiles. Figure 7b shows that the transition between boundary layer inflow (negative velocities) and outflow (positive velocities) is generally between 600- and 1000-m altitudes. Between  $-5$ - and  $+2.5$ -km distance from coast the height of the inflow layer appears to increase relative to the surrounding bins. However, the inflow from 800 to 1000 m is very weak and is near the 10% criteria, suggesting that by definition the inflow depth is relatively constant across the coastal interface in this analysis. On the other hand, farther inland the vertical distance between the maximum tangential wind and the top of the inflow layer appears to diminish from over water to onshore. Between  $-10$  and  $-5.0$  km, the height of the maximum tangential

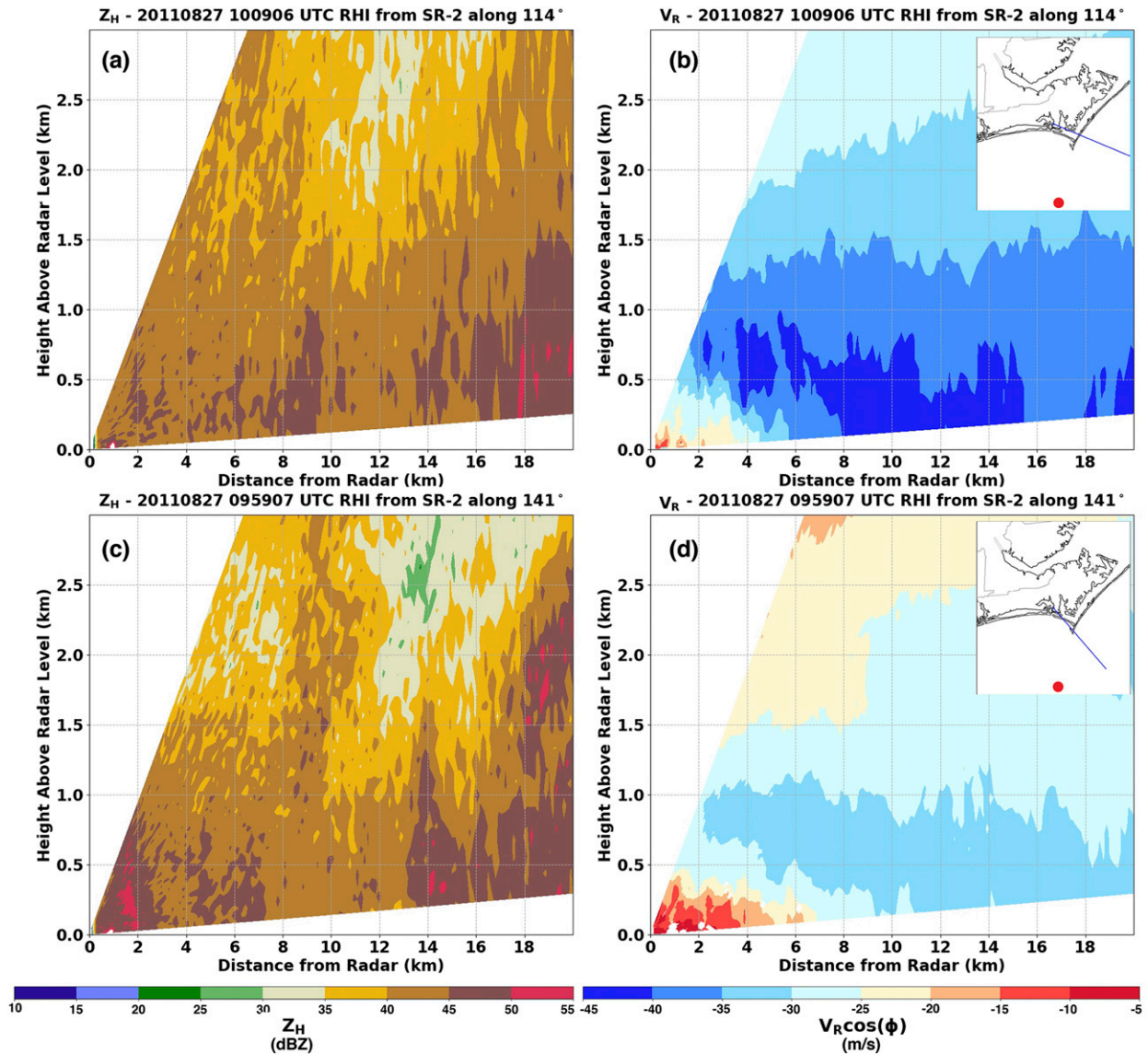


FIG. 6. RHI from SMART radar 2 along an azimuth of (a),(b) 114° from north at 1009 UTC and (c),(d) 141° from north at 0959 UTC. (a),(c) Radar reflectivity in dBZ, according to the color scale, in the plane of the RHI is shown. (b),(d) Radial velocity is shown projected into the horizontal according to the elevation along which it was taken. A plan view of the RHI (blue line) and 1000 UTC location of Irene’s center (red circle) is overlain upon a map of the coastal region in the inserts of (b) and (d). It should be noted that at 1009 (0959) UTC the 8 (6)-km range is approximately representative of the shoreline of the greater continental region and 18 (8.5) km is approximately the shoreline of the North Carolina barrier islands.

wind resides in the mean outflow layer, which is above the HBL top.

*c. Coastal composite change*

Since the evolution of the normalized winds is a function the mean wind, it is useful to characterize the HBL transition in terms of the maximum normalized wind to more comprehensively view the HBL transition at the coastal interface. A time-averaged VAD profile from KMHX taken over the same period as the dual-Doppler analyses is

used as a proxy for the HBL downstream of the  $-10$ - to  $-7.5$ -km range bin in Fig. 5a. The individual VADs used in the composite were normalized by the 200–600-m wind to be consistent with the dual-Doppler normalized profiles. Then, for each composite profile (KMHX and each range bin in Fig. 5a), the maximum normalized wind was found and the profile was shifted such that the maximum normalized wind was represented by a value of 1.0 (Fig. 8a). It is clear that the profiles above 800-m altitude adjust little, while the profiles below evolve rapidly as a function of

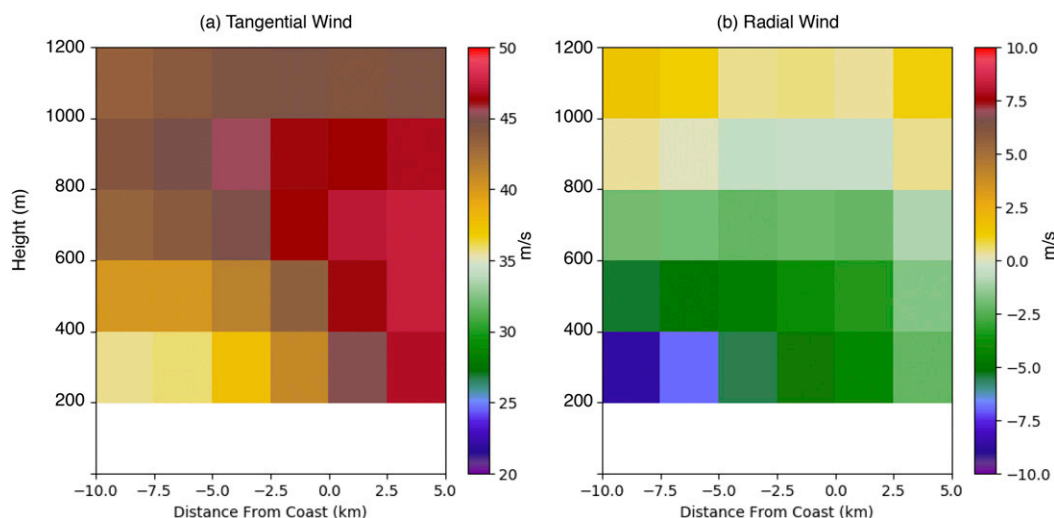


FIG. 7. Full (not normalized) average coast-relative (a) tangential and (b) radial wind speeds ( $\text{m s}^{-1}$ ) according to the color bars. Negative values indicate storm-relative inflow in (b).

inland distance. This is indicative of IBL growth, as expected across the coast. The top of the “kink” in the profile below the otherwise unaffected winds aloft can be used as a proxy for the height of the growing IBL, which suggests rapid growth of the IBL within 5 km of the coast and relatively slow growth farther inland.

However, the adjustment of the HBL to the inland surface roughness regime implies that the HBL wind profile through the coastal transition may deviate from a logarithmic profile (or log-linear profile). Over the ocean on average, dropsonde profiles suggest that the HBL is indeed log linear (e.g., Franklin et al. 2003; Powell et al. 2003; Giammanco et al. 2013). This notion is examined via the dual-Doppler coastal-composite analyses by computing the aerodynamic surface roughness needed to maintain a log-linear profile between 200 m (the lowest available dual-Doppler wind measurement) and the height of the maximum wind (calculated for each profile as a function of distance from the coast). This calculation is done via the time-average full wind speed, not the normalized wind speed. Following the general technique of Kosiba et al. (2013) and Alford et al. (2019) using a wind speed at 200-m  $V_{200}$  and the maximum wind speed  $V_{\max}$  at a height of  $z_{\max}$ , the aerodynamic surface roughness  $z_0$  can be calculated by solving for  $z_0$  in (2) to obtain (3):

$$V_{200} \ln(200/z_0) = V_{\max} \ln(z_{\max}/z_0), \quad (2)$$

$$z_0 = \exp\{[V_{\max} \ln(200) - V_{200} \ln(z_{\max})]/(V_{\max} - V_{200})\}. \quad (3)$$

The resulting  $z_0$  are indicated in Fig. 8b, which range from  $<0.001$  for over-water surfaces and 0.001 to 0.37

for over-land surfaces, which appear to be reasonable averaged across relatively large spatial areas with complex land-use conditions. More importantly, the profiles between 200 m and  $z_{\max}$  remain mostly log linear, suggesting that the IBL through the coastal transition remains representative in general of a logarithmic boundary layer.

## 5. Temporal evolution of the coastal HBL

Previous studies often employ the use of mean profiles (as above) to assess the structure of the HBL, either over land or over water. However, the evolution of the HBL in storm-center-relative space has not been examined quantitatively to our knowledge. Here, we examine the temporal evolution of the HBL over land compared to that observed over water using dual-Doppler analyses and available VAD retrievals from RaXPOL and KMHX.

### a. Dual-Doppler analysis results

Using a time series of area-averaged normalized vertical wind profiles, the transition of the mean boundary layer wind speed and depth over land and over water in the dual-Doppler domain can be ascertained. As we discuss the wind speeds in their normalized forms, the area-mean 0–600-m winds are shown in Fig. 4c (Fig. 4d) for land (water) surfaces. However, each dual-Doppler profile at each dual-Doppler analysis grid point is normalized by its own 0–600-m mean wind. Thus, the mean winds shown in Figs. 4c and 4d are for general context only. In Fig. 9, time periods from approximately 0000 to 0716 UTC 27 August represent the outer bands of Irene, 0716–1046 UTC represents the inner core, and 1046–1206 UTC represents the eyewall. These spatial



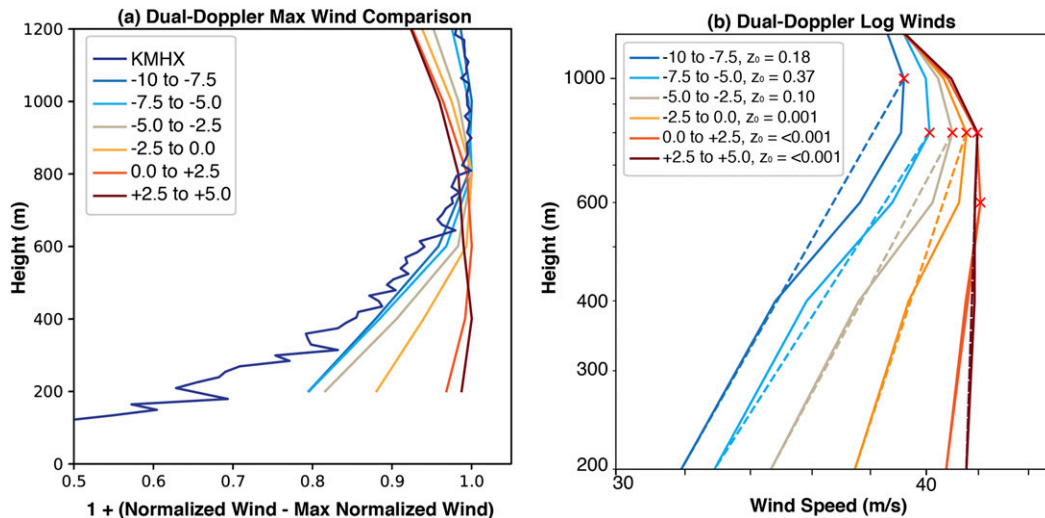


FIG. 8. (a) A comparison of the coast-relative normalized boundary layer profiles from Fig. 5 and average boundary layer normalized profiles for VADs retrieved from KMHX. The coast-relative distance is indicated according to the contour color in the inset legend. A value of 1.0 indicates the maximum wind. (b) The mean boundary layer winds (full; solid curves) compared to a logarithmic profile constructed between the maximum wind (red  $\times$  symbols) and 200 m. The roughness length  $z_0$  is shown in the legend and represents the value required to maintain a log-linear profile between the maximum wind and the 200-m wind.

regions were defined by the spatially averaged  $r^*$  over the dual-Doppler domain. Normalized radii larger than 3 were considered to be outer bands, 1.5–3 was considered inner core, and 0.8–1.5 was considered eyewall. Within each of these regions, the structures of the profiles for each regime (outer bands, inner core, and eyewall) differ strongly from one another. The normalized 0–1200-m wind profiles indicate that the strongest boundary layer winds are generally experienced between 400- and 1200-m heights for all inland profiles, but the height of the maximum wind descends with decreasing radial distance (increasing time) to the eyewall, namely, in the inner-core and eyewall regimes. Below the inland maximum winds (Fig. 9a), the normalized wind at the lowest analysis level between 0000 and 0700 UTC (outer bands) is generally weaker than in the inner-core and eyewall regimes. Additionally, the winds above the maximum in the inner-core and eyewall regimes decrease rapidly, which is generally not seen in the outer band regime, indicative of a jet-like profile in the eyewall of Irene. A similar trend is seen in over-water profiles, but with stronger mean-wind-relative reductions above the wind maximum during the inner core and eyewall, indicative of a more pronounced wind maximum (i.e., jet-like profile; Fig. 9b). This trend has been observed in over-water mean profiles in other studies (Franklin et al. 2003; Giammanco et al. 2013). The inner-core regime after  $\sim$ 0700 UTC for both land and water profiles shows greater temporal consistency of a jet-like profile in the

boundary layer and a gradual decrease in the height of the maximum wind toward the eyewall. As mentioned, the eyewall exhibits a more classic “jet” profile (e.g., Kepert 2001) with maximum normalized winds near 400-m heights over water and 600–800 m inland. Thus, the dual-Doppler analyses reveal unique HBL structures in the outer band, inner core, and eyewall regimes that are qualitatively similar inland and over water, but quantitatively different especially in the lowest analysis levels, where the decay of the wind below the maxima is much greater for inland profiles. In addition, the normalized wind speeds at 200–400 m are notably less than 0.9 for most inland profiles (excluding the eyewall) and generally greater than 0.95 for over-water profiles.

Wind direction for land and water surfaces in the vertical was also examined (Figs. 9e,f). In all regimes, wind directions over land varied between  $\sim$ 60° and  $\sim$ 90° (from the north) at the lowest analysis levels and turned clockwise with height. Similar trends were seen in the over-water profiles of wind direction (Fig. 9f). While above 600–800 m little difference was found quantitatively in the wind direction for each domain subset, below 600-m altitude a counterclockwise change in the wind direction of 10°–20° onshore was observed, similar to the results of Hirth et al. (2012). However, the magnitude of the counterclockwise wind direction change from over-water to over-land profiles is generally greater in the outer bands and the outer edge of the inner core (differences of 10°–15° from 0000 to

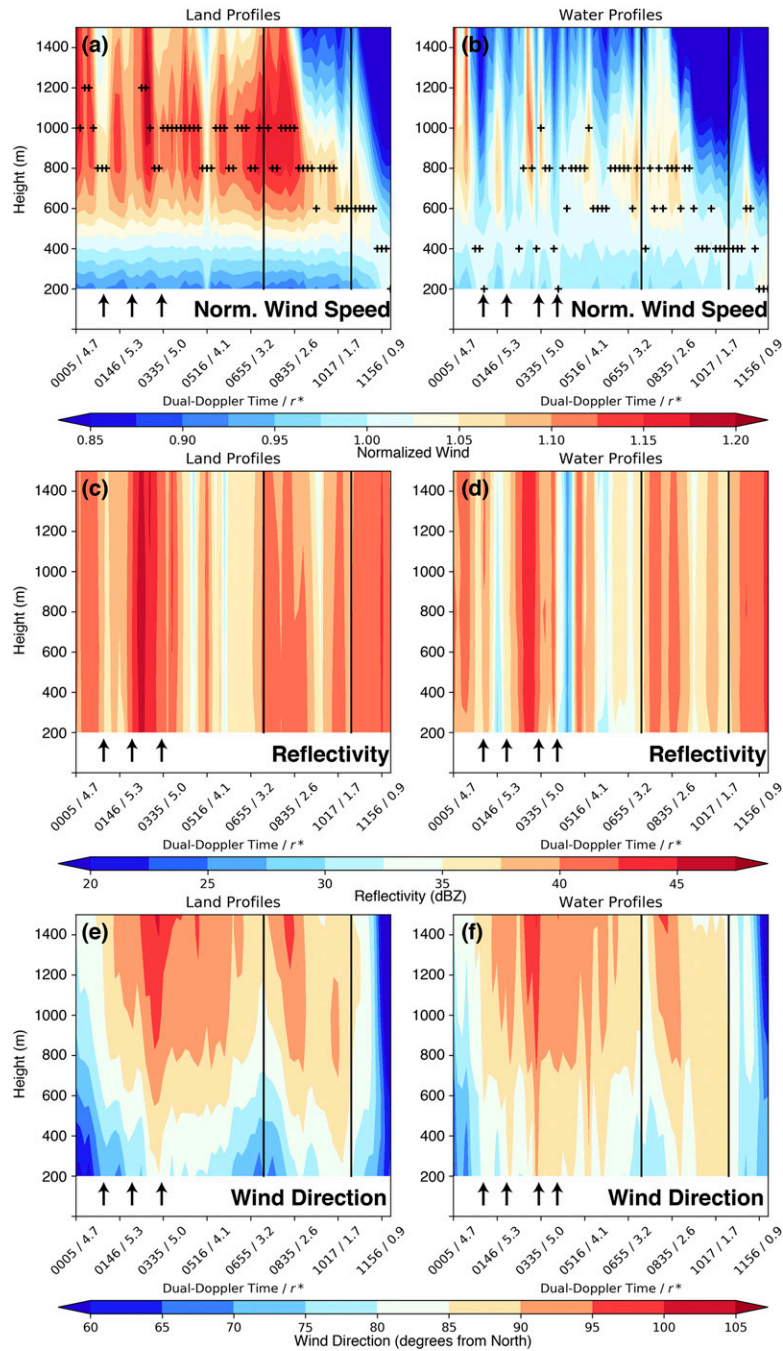


FIG. 9. Normalized wind profiles (a) over land and (b) over water within the dual-Doppler analysis domain subset shown in Fig. 4. The labels along the  $x$  axis indicate the dual-Doppler time and the area-mean normalized radius  $r^*$ . Profiles are constructed for each dual-Doppler time ( $x$  axis) in height ( $y$  axis). The values of the normalized wind are shown according to the color bar at the bottom of the figure. The black lines indicate the separation of the outer bands-inner core regime at  $r^* = 3.0$  and the separation of the inner core-eyewall regime at  $r^* = 1.5$ . The black plus signs indicate the height of the maximum normalized wind. (c),(d) Land and water profiles of area-mean reflectivity, respectively. (e),(f) Area-mean profiles of wind direction with height for land and water profiles, respectively. The arrows in the figure depict periods of increased normalized winds in (a) and (b), their corresponding periods of changing reflectivity in (c) and (d), and their corresponding changes in wind direction in (e) and (f).

0830 UTC) than in the inner-core and eyewall regimes ( $5^{\circ}$ – $10^{\circ}$  from 0835 to 1200 UTC).

Several transient maxima in the 200–400-m normalized wind can be seen both over land and over water in the outer-band regime (Figs. 9a,b), suggesting that the winds relative to the boundary layer mean increase in, perhaps, rainbands. Changes in the wind direction (Figs. 9e,f) and relative peaks in area-averaged wind speeds (Figs. 4c,d) can also be seen corresponding to changes in the low-level wind structure. Area-averaged radar reflectivity was computed to provide a proxy for periods when the dual-Doppler domain was under the influence of outer rainbands. For low-level (<400 m) normalized wind maxima in the outer band regime (annotated by arrows in Fig. 9), reflectivity was generally reduced relative to its surrounding values, suggesting that low-level normalized wind maxima (Figs. 9a,b), domain-averaged 0–600-m mean wind (Figs. 4c,d), and wind direction changes (Figs. 9e,f) were experienced on the edges of rainbands (Figs. 9c,d). When the area-averaged reflectivity was at a local maximum, the normalized winds often maximized aloft. This result is similar to the results of Ming et al. (2014), who showed that downward turbulent fluxes were often maximized on the exterior of rainbands, leading to the downward transport of high momentum. Retrieved vertical velocity was also explored, but did not show significant trends in an area-averaged sense.

### b. RaXPOL VAD profiles

To explore the structure of the outer-band regime in greater detail, the structure of the HBL can be examined through VAD retrievals approximately every 30 s to 1 min during the RaXPOL operational period. The radial and temporal resolution of RaXPOL affords the opportunity to explore the low-level perturbations to the HBL structure (Fig. 9) and increases in the area-average winds (Fig. 4) that may be associated with rainbands. While turbulence on a variety of scales can also influence the vertical distribution of momentum (Morrison et al. 2005; Lorsolo et al. 2008; Kosiba and Wurman 2014; Zhang et al. 2008, 2011), we focus specifically on rainbands here. Based on the time series of dual-Doppler domain-averaged HBL structure, it was shown that local maxima in the normalized wind profiles were often associated with gradients in the domain-averaged reflectivity.

In Fig. 10, a similar time series is shown for 0000 to 0500 UTC documenting the VADs retrieved from radial velocity observations. Figure 10a shows the time series of VAD-derived winds from 0 to 1200 m at 15-m vertical resolution. Local maxima (minima) in the low levels can be seen and are denoted by solid (dashed) rectangles in

Fig. 10a. During these periods, winds in the lowest 100 m of the profiles tend to be between  $15$  and  $20 \text{ m s}^{-1}$  relative to surrounding local minima of  $10$ – $15 \text{ m s}^{-1}$ . These local minima appear to be sometimes in the presence of local maxima aloft, suggesting that high-momentum air is seen during these periods at lower levels relative to surrounding times through the observed column.

The reflectivity structure observed by RaXPOL was examined in context of these wind maxima (minima) to deduce if rainband and convective structures were responsible for these perturbations to the wind field. For the example times denoted in Fig. 10a, the wind maxima (minima) are highlighted in Fig. 10b over the vertical reflectivity structure. During the periods of local wind maxima denoted in the figure, rainband passage is observed in the vertical structure of the reflectivity. To a degree in the low levels (denoted by black rectangles in Fig. 10a) and in the upper levels (denoted by black ovals in Fig. 10a) of the VAD profiles, the wind maxima appear to be offset from the reflectivity maxima, suggesting that many of the local wind maxima are experienced on the edges of deep convection. One maximum between 0033 and 0045 UTC appears to be in a core of reflectivity, which resembles precipitation-induced downdrafts previously seen in airborne kinematic retrievals of convection in the outer bands (Barnes et al. 1983, 1991). This suggests larger-scale kinematic rainbands and/or convective-scale kinematics are responsible for the low-level perturbations to the wind field. Particularly for the local maxima observed aloft, these appear to resemble the wind field perturbations observed by the spatially averaged time series of dual-Doppler analyses in the outer bands (Fig. 9). Since the perturbations exist primarily on gradients in reflectivity where downdrafts are anticipated, we expect that the downward flux of high momentum as in Ming et al. (2014) is likely an important mechanism for the local enhancements to the near-surface winds. It has also been observed that gust factors are higher in rainbands (e.g., Schroeder et al. 2009; Giammanco et al. 2016), to which this analysis lends support. As the dual-Doppler composite results and VADs represent horizontal scales of flow larger than, for example, HBL rolls (e.g., Kosiba and Wurman 2014), we interpret the results here as predominantly associated with larger-scale (i.e., rainband) processes. Nevertheless, we anticipate that smaller-wavelength features in the HBL also contribute perturbations to the HBL wind structure, which will be discussed in section 6.

### c. KMHX VAD profiles

The coastal WSR-88D was downstream from the profiles discussed in section 4b, suggesting that its



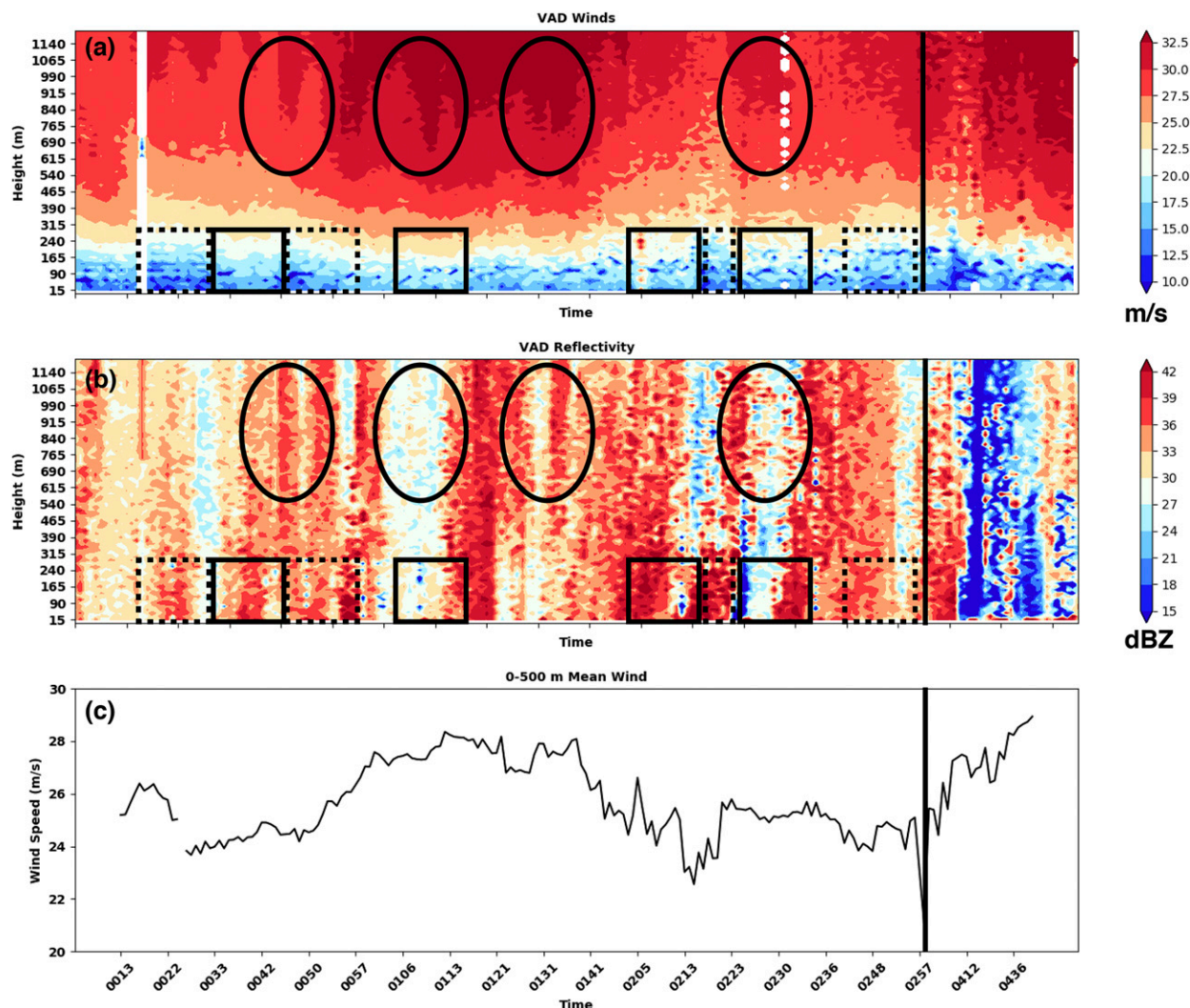


FIG. 10. Time series of RaXPol-observed HBL structure from 0013 to 0500 UTC. (a) VAD-derived winds as a function of height ( $y$  axis) over time ( $x$  axis). Wind speeds (total) are shown according to the color bar to the right of (a). (b) As in (a), but for the vertical profile of radar reflectivity. (c) The VAD-derived 0–500-m mean wind is shown for context. In both (a) and (b), the black solid (dashed) rectangles indicate example periods during which there are local wind maxima (minima) in the lower part of the VAD profiles. The black ovals indicate periods of wind maxima in the upper part of the VAD profiles. The vertical black line denotes a temporal gap in RaXPol data.

time varying mean profiles can be used to characterize wind profiles farther inland relative to those within 10 km of the coastline (approximately 18 km from the nearest saltwater inlet to KMHX's north). A time series of VADs from KMHX (Fig. 11) was constructed to compare the normalized boundary layer winds to the dual-Doppler area-averaged time series shown in Fig. 9a. Indeed, the KMHX VADs replicate the regimes observed in the dual-Doppler results well. Between 0000 and around 0730 UTC, the normalized winds are maximized near 1000 m. Between  $\sim$ 0730 and  $\sim$ 1030 UTC, the inner-core regime shows maximum winds between 600 and 850 m, similar to the dual-Doppler analysis

results. Finally, the eyewall regime after  $\sim$ 1030 UTC shows the maximum normalized wind near 700 m initially and decreases in height to 300–500 m nearer 1200 UTC. Relatively stronger normalized flow also characterizes the low levels of the retrievals compared to earlier times. However, the magnitude of the  $\sim$ 200-m normalized wind is greater in the VADs than in the dual-Doppler analysis results due to the contribution of the winds below 200 m to the 0–500-m boundary layer mean wind. The VAD winds near 200 m are characterized by values near 100% of the mean wind rather than 0.9 or less in the dual-Doppler analyses (Fig. 9a). The lowest analysis level (representative of 50–65-m altitude)



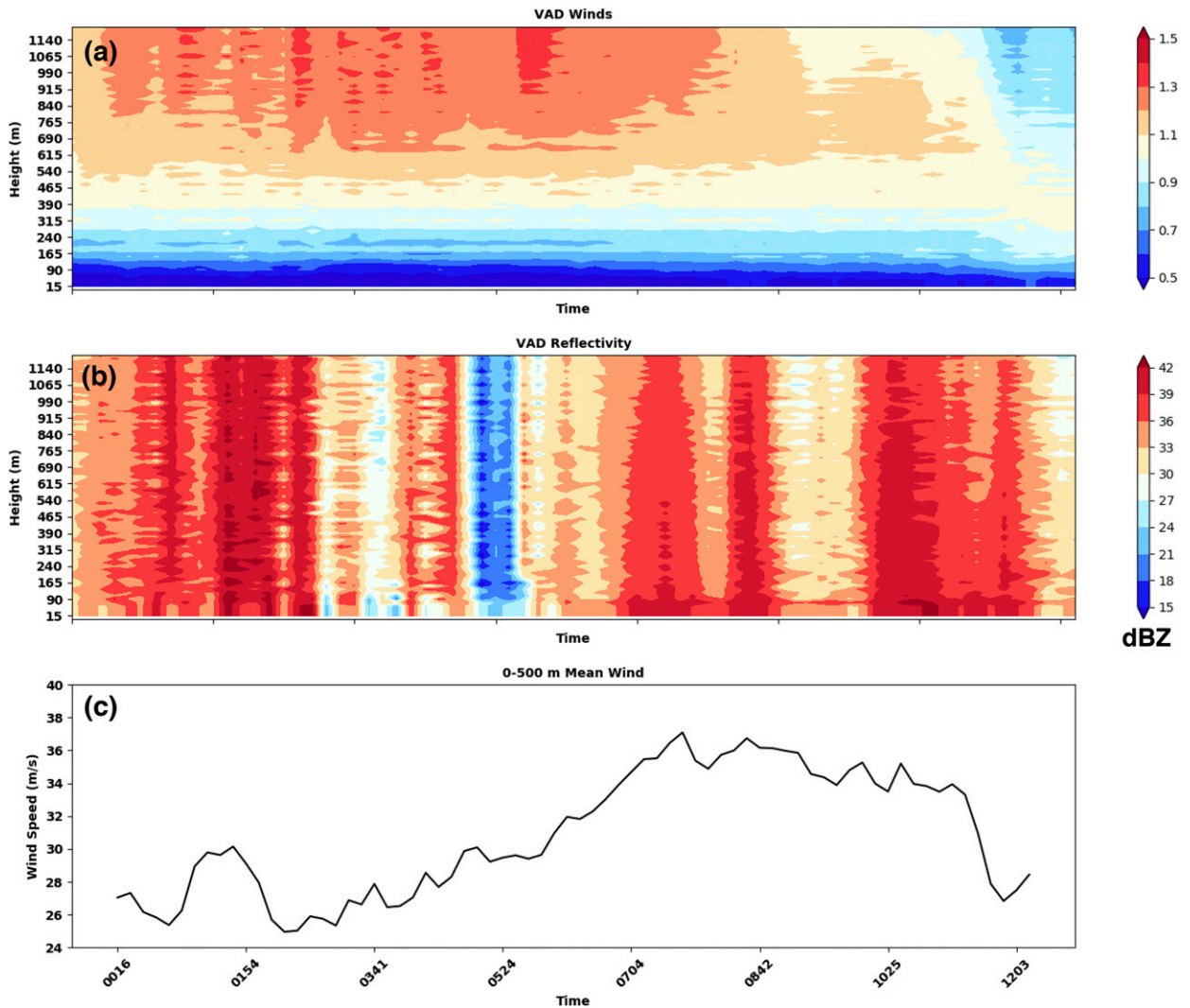


FIG. 11. Time series of KMHX VAD profiles as in Fig. 10. (a) As in Fig. 10a, but for the normalized wind.

suggests that the winds in the outer bands fluctuate between 50% and 60% of the mean wind (with similar time varying perturbations seen to those characterized by the RaXPoL VADs and dual-Doppler time series). In the inner core and eyewall, however, the magnitude of the 70–120-m normalized wind increases to 65%–75% of the boundary layer mean at times.

Delineated by distance to the center of circulation, Figs. 12 and 13 show the VAD-derived boundary layer winds averaged over time for radial and tangential profiles, respectively. Unlike the dropsonde profiles (Figs. 3c,d), the radial winds derived from KMHX exhibit a layer of maximum radial inflow above the surface (generally between 200 and 400 m). The normalized tangential profiles (not shown) indicate that the 200–400-m winds are generally 90%–100% of the boundary layer mean wind, similar to the dual-Doppler and

VAD results discussed previously. The dual-Doppler coast-relative composites suggest that the maximum tangential wind speed first resides in or near the top of the inland HBL within 5 km of the coast, but transitions to above the HBL 5–10 km inland. Given that KMHX is downstream of the dual-Doppler observations and farther inland, the maximum tangential wind speed should also be expected to reside near or above the HBL. Indeed, within 100 km of the storm's center of circulation (Figs. 12a,b and 13a,b), the height of the inflow layer and the maximum tangential wind speed is approximately at the same altitude (600 m). For profiles taken farther away from the storm center, (Figs. 12c,d and 13c,d), maximum tangential wind height (800–1000 m) is well above the top of the HBL. This suggests that the vertical displacement between the maximum tangential wind and the top of the

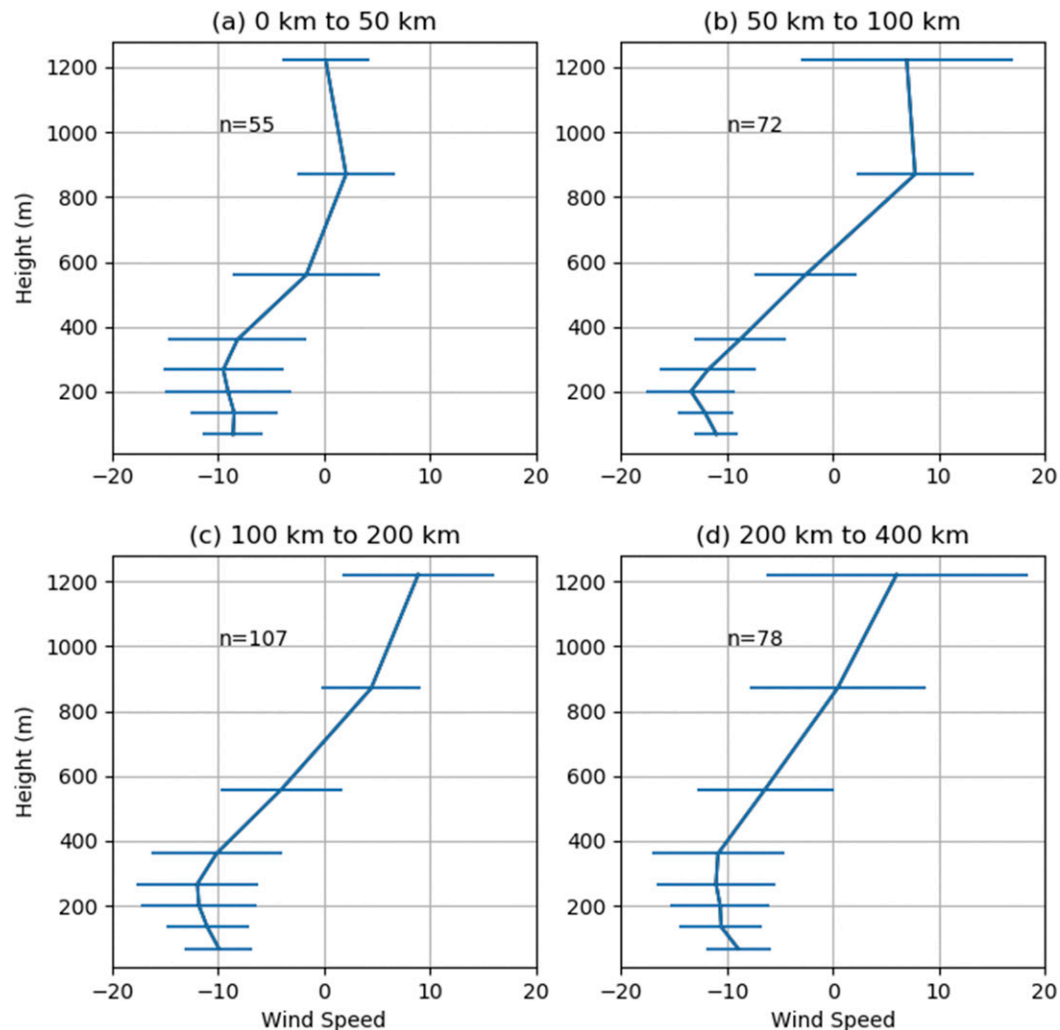


FIG. 12. Radial wind profiles ( $\text{m s}^{-1}$ ) derived from the KMHX VAD analysis. Profiles are shown (a) 0–50, (b) 50–100, (c) 100–200, and (d) 200–400 km from the center of circulation of Irene.

HLB increases with distance from the center of circulation over land.

## 6. Discussion and conclusions

As found in Ming et al. (2014) and Marks et al. (2020, manuscript submitted to *Mon. Wea. Rev.*), the height of the boundary layer over land is increased relative to the over-ocean boundary layer structure and resides above the inflow layer. Prior studies such as Ming et al. (2014) suggest that the tangential wind maximum above the inflow layer is a direct consequence of the adjustment of the HBL to changing surface characteristics (i.e., IBL growth). However, the process by which the HBL transitions across the coastal region was not documented. Hirth et al. (2012) showed that the coastal region represents a discontinuity in surface

roughness. Their work focused on HBL change observed inland, but offered limited comparison of the HBL structure over water.

Here, using high-spatial-resolution observations of the HBL relative to the coastline, the transition of the boundary layer characteristics at the coastal interface were examined, which resulted in several key conclusions:

- 1) Using a unique dropsonde, dual-Doppler, and VAD dataset, quantitative differences in the HBL winds were documented. It was shown that the evolution of the HBL was qualitatively similar over water and over land, but their magnitudes were significantly different for all regimes (outer bands, inner core, and eyewall).
- 2) Past studies focused on VAD or boundary layer profiler (i.e., point profiles) retrievals have shown that downdrafts on the periphery of outer rainbands can lead to a reduction in the height of the maximum

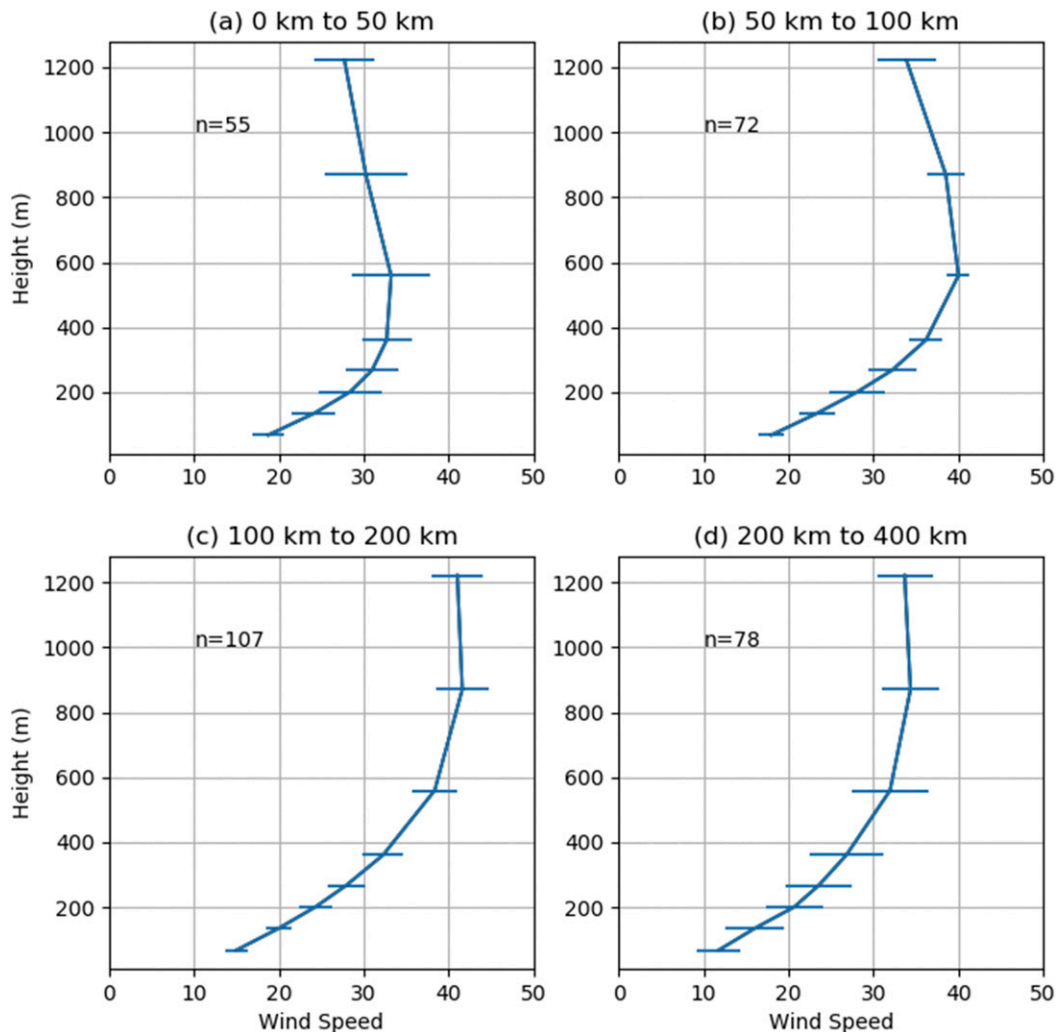


FIG. 13. As in Fig. 12, but for the tangential wind.

wind. Based on the mean structure throughout the dual-Doppler domain corroborated by coincident VAD retrievals, this dataset suggests that rainbands are indeed responsible for an enhancement in the lower-HBL winds.

- 3) VAD-based studies have suggested that the maximum wind over land resides atop the HBL, rather than within it as over the open ocean. The data herein document that the growth of the IBL is directly responsible for mixing out the previous tangential maximum over the open ocean, wherein the tangential winds above the newly adjusted IBL/HBL become the maximum.
- 4) As the IBL grows, the wind profile below the maximum likely remains mostly logarithmic as the HBL responds to the inland, large-scale surface roughness change.

Figure 14 summarizes the key observations that resulted from this analysis. Between 0 and 5 km over water

the maximum tangential wind was observed to reside in the inflow layer (HBL; see Fig. 7) similar to past observations near the coast and over shallow and deep water (e.g., Zhang et al. 2011; Hirth et al. 2012). In the first 5 km inland of the coast, the height of the maximum tangential wind (Fig. 7a) is still within the inflow (boundary layer; Fig. 9b) as the HBL responds to the discontinuity in surface roughness at the coast (i.e., IBL growth; Fig. 14). However, these results suggest that the residual boundary layer does not immediately adjust to the underlying surface, similar to the results of Hirth et al. (2012). Thus, for a period the tangential wind maximum may continue to reside in the inflow layer until the HBL over land has fully adjusted to its underlying surface (Fig. 14). RHIs from SR2 support that the adjustment of the HBL begins rapidly in the first few kilometers inland of the coast, similar to the mean coast-relative profiles. The  $V_R$  maximum observed

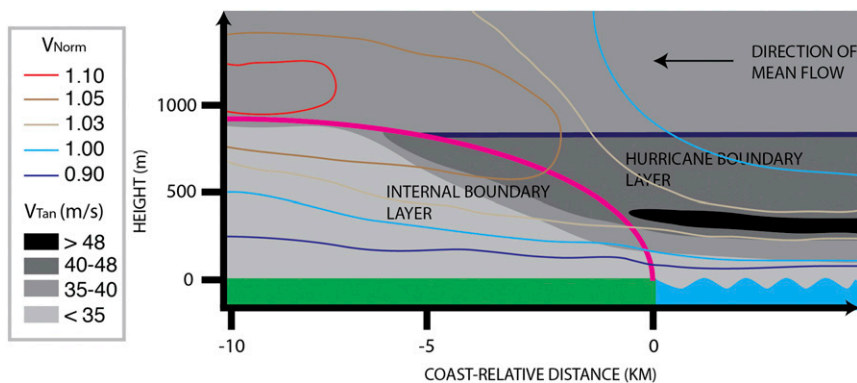


FIG. 14. Conceptual model of the HBL transition across the coastal interface for Hurricane Irene. The dark blue line represents the height of the pre-existing HBL that results from HBL dynamics over the open ocean. The magenta curve represents the growth of the internal boundary layer response to the surface roughness discontinuity at the coast. The tangential wind  $V_{tan}$  is shown via the color-filled contours according to the legend. The line contours according to the legend indicate the approximate value of the mean state of the coast-relative normalized wind  $V_{Norm}$ . The mean flow is directed from right to left (toward the coast).

in the lowest 500 m of the RHIs over water appeared to increase in height onshore where the IBL growth was occurring. Alford et al. (2019) and Fernández-Cabán et al. (2019), for example, showed that convective perturbations in the eyewall can represent the strongest winds during the landfall process. Downdrafts in the region may more readily project stronger momentum aloft in the near-coastal regions toward the surface prior to the full adjustment of the HBL to the increased surface roughness inland of the coast. While most observational studies suggest that gust factors immediately inland of the coast do not significantly depart from the mean, Giammanco et al. (2016) support the notion that the wind maximum within the HBL is, perhaps, an upper bound on the magnitude surface winds. Additional data are needed, however, to fully explore this idea. However, changes in the boundary layer structure in time (Figs. 9 and 10) are indeed noted in the outer bands, where rainband passage procures the strongest winds in the low levels relative to their boundary layer means in a domain-wide sense. This study focused on larger-scale structures that can be examined through the mean HBL structure, rather than kilometer and subkilometer features that also impact the vertical distribution of horizontal momentum (Morrison et al. 2005; Lorsolo et al. 2008; Zhang et al. 2008; Kosiba and Wurman 2014). This topic will be addressed in future work.

This work augments the mean profile studies referenced herein, which show a strong reduction in the near-surface boundary layer wind relative to its peak aloft. Here, it is found that periods of convection result in greater linearity of the boundary layer profile over water

above 200 m as shown by dual-Doppler analysis (e.g., Fig. 9). While dual-Doppler observations cannot be used to directly retrieve the standardized 10-m wind, the result suggests that preconvective periods may procure the strongest near-surface winds in the outer bands, supported by the lower-level retrievals procured by RaXPoL and KMHX VADs. Based on past studies, greater downward momentum flux on the edges of convection in the outer bands is likely responsible for the transition of a sharply decreasing profile relative to the boundary layer maximum wind to a gradual reduction in the boundary layer wind relative to its above maximum. In contrast, perturbations to the low-level winds were not seen in the inner-core regime, but the height of the maximum wind was indeed reduced between the outer bands and the inner core. The eyewall regime transitioned to a strong jet-like profile with a maximum below 500 m in this case. The highest normalized winds in the lowest 100 m of the atmosphere were found in the eyewall regime retrieved by VADs from KMHX. Although addressed to some degree, it is still unclear how the winds near the surface (10-m altitude) evolve relative to the mean winds aloft due to a lack of high resolution (e.g., 200–250-m resolution) dual-Doppler analyses (Krupar et al. 2016). While Krupar et al. (2016) found that a logarithmic profile did not represent the HBL as well as a linear-regression fit, this work suggests a log profile was generally applicable in Hurricane Irene at dual-Doppler analysis levels. Thus, future work should focus on characterizing the complete boundary layer structure from the surface through the top of the HBL onshore and near the shore. As the Texas Tech University StickNets and FCMP 10-m towers were



available during the landfall of Irene, our dataset is ideal for comparison in a future study.

This work represents a high-spatiotemporal-resolution observational case study in a gradually weakening TC, but emphasizes the need for additional observations of the boundary layer during TC landfalls. The general conclusions from this work should be studied in stronger storms to assess the generality of the results across various TC intensities. Over the open ocean, boundary layer structure is not only a function of radial distance from the eyewall or shear-relative quadrants, but also a function of TC intensity. Thus, we anticipate similar results may also apply at landfall.

*Acknowledgments.* This work was partially supported by RAPID Grants AGS-1759479 and AGS-1902593 from the National Science Foundation and by the National Institute of Standards and Technology under Grant 70NANB19H056. We also thank three anonymous reviewers for their constructive comments that improved the quality of this manuscript. The first author was supported by NASA Headquarters under the NASA Earth and Space Science Fellowship Program—Grants 17-EARTH17R-72 and 18-EARTH18R-0086. Jun Zhang was supported by NSF Grant AGS1822128 and NOAA Grant NA14NWS4680030. NOAA authors were also supported by AOML/HRD. SMART radar data and RaXPol VADs are available at the Zenodo Archive doi: [10.5281/zenodo.3494891](https://doi.org/10.5281/zenodo.3494891). HRD archived dropsondes are available at [https://www.aoml.noaa.gov/hrd/data\\_sub/](https://www.aoml.noaa.gov/hrd/data_sub/). RaXPol is maintained and operated by the Advanced Radar Research Center (ARRC) of the University of Oklahoma.

#### REFERENCES

- Aberson, S. D., and J. L. Franklin, 1999: Impact on hurricane track and intensity forecasts of GPS dropwindsonde observations from the first-season flights of the NOAA Gulfstream-IV jet aircraft. *Bull. Amer. Meteor. Soc.*, **80**, 421–427, [https://doi.org/10.1175/1520-0477\(1999\)080<0421:IOHTAI>2.0.CO;2](https://doi.org/10.1175/1520-0477(1999)080<0421:IOHTAI>2.0.CO;2).
- , M. L. Black, R. A. Black, R. W. Burpee, J. J. Cione, C. W. Landsea, and F. D. Marks, 2006: Thirty years of tropical cyclone research with the NOAA P-3 aircraft. *Bull. Amer. Meteor. Soc.*, **87**, 1039–1056, <https://doi.org/10.1175/BAMS-87-8-1039>.
- Alford, A. A., M. I. Biggerstaff, G. D. Carrie, J. L. Schroeder, B. D. Hirth, and S. M. Waugh, 2019: Near-surface maximum winds during the landfall of Hurricane Harvey. *Geophys. Res. Lett.*, **46**, 973–982, <https://doi.org/10.1029/2018GL080013>.
- Avila, L. A., and J. Cangialosi, 2012: Tropical cyclone report: Hurricane Irene (AL092011), 21–28 August 2011. NHC Tech. Rep., 45 pp., [http://www.nhc.noaa.gov/data/tcr/AL092011\\_Irene.pdf](http://www.nhc.noaa.gov/data/tcr/AL092011_Irene.pdf).
- Barnes, G. M., E. J. Zipser, D. Jorgensen, and F. Marks, 1983: Mesoscale and convective structure of a hurricane rainband. *J. Atmos. Sci.*, **40**, 2125–2137, [https://doi.org/10.1175/1520-0469\(1983\)040<2125:MACSOA>2.0.CO;2](https://doi.org/10.1175/1520-0469(1983)040<2125:MACSOA>2.0.CO;2).
- , J. F. Gamache, M. A. Lemone, and G. J. Stossmeister, 1991: A convective cell in a hurricane rainband. *Mon. Wea. Rev.*, **119**, 776–794, [https://doi.org/10.1175/1520-0493\(1991\)119<0776:ACCIAH>2.0.CO;2](https://doi.org/10.1175/1520-0493(1991)119<0776:ACCIAH>2.0.CO;2).
- Betten, D. P., M. I. Biggerstaff, and C. L. Ziegler, 2018: Three-dimensional storm structure and low-level boundaries at different stages of cyclic mesocyclone evolution in a high-precipitation tornadic supercell. *Adv. Meteor.*, **2018**, 9432670, <https://doi.org/10.1155/2018/9432670>.
- Biggerstaff, M. I., and Coauthors, 2005: The Shared Mobile Atmospheric Research and Teaching radar: A collaboration to enhance research and teaching. *Bull. Amer. Meteor. Soc.*, **86**, 1263–1274, <https://doi.org/10.1175/BAMS-86-9-1263>.
- , Z. Zounes, A. A. Addison, G. D. Carrie, J. T. Pilkey, M. A. Uman, and D. M. Jordan, 2017: Flash propagation and inferred charge structure relative to radar-observed ice alignment signatures in a small Florida mesoscale convective system. *Geophys. Res. Lett.*, **44**, 8027–8036, <https://doi.org/10.1002/2017GL074610>.
- Browning, K. A., and R. Wexler, 1968: The determination of kinematic properties of a wind field using Doppler radar. *J. Appl. Meteor.*, **7**, 105–113, [https://doi.org/10.1175/1520-0450\(1968\)007<0105:TDOKPO>2.0.CO;2](https://doi.org/10.1175/1520-0450(1968)007<0105:TDOKPO>2.0.CO;2).
- Bryan, G. H., and R. Rotunno, 2009: The maximum intensity of tropical cyclones in axisymmetric numerical model simulations. *Mon. Wea. Rev.*, **137**, 1770–1789, <https://doi.org/10.1175/2008MWR2709.1>.
- Crum, T. D., and R. L. Alberty, 1993: The WSR-88D and the WSR-88D operational support facility. *Bull. Amer. Meteor. Soc.*, **74**, 1669–1687, [https://doi.org/10.1175/1520-0477\(1993\)074<1669:TWATWO>2.0.CO;2](https://doi.org/10.1175/1520-0477(1993)074<1669:TWATWO>2.0.CO;2).
- Elliott, W. P., 1958: The growth of the atmospheric internal boundary layer. *Eos, Trans. Amer. Geophys. Union*, **39**, 1048–1054, <https://doi.org/10.1029/TR039i006p01048>.
- Fernández-Cabán, P. L., and Coauthors, 2019: Observing Hurricane Harvey’s eyewall at landfall. *Bull. Amer. Meteor. Soc.*, **100**, 759–775, <https://doi.org/10.1175/BAMS-D-17-0237.1>.
- Franklin, J. L., M. L. Black, and K. Valde, 2003: GPS dropwindsonde wind profiles in hurricanes and their operational implications. *Wea. Forecasting*, **18**, 32–44, [https://doi.org/10.1175/1520-0434\(2003\)018<0032:GDWPIH>2.0.CO;2](https://doi.org/10.1175/1520-0434(2003)018<0032:GDWPIH>2.0.CO;2).
- Garratt, J. R., 1990: The internal boundary layer—A review. *Bound.-Layer Meteor.*, **50**, 171–203, <https://doi.org/10.1007/BF00120524>.
- Giammanco, I. M., J. L. Schroeder, and M. D. Powell, 2013: GPS dropwindsonde and WSR-88D observations of tropical cyclone vertical wind profiles and their characteristics. *Wea. Forecasting*, **28**, 77–99, <https://doi.org/10.1175/WAF-D-11-00155.1>.
- , —, F. J. Masters, P. J. Vickery, R. J. Krupar, and J. A. Balderrama, 2016: Influences on observed near-surface gust factors in landfalling U.S. Gulf Coast hurricanes: 2004–08. *J. Appl. Meteor. Climatol.*, **55**, 2587–2611, <https://doi.org/10.1175/JAMC-D-16-0053.1>.
- Halverson, J. B., J. Simpson, G. Heymsfield, H. Pierce, T. Hock, and L. Ritchie, 2006: Warm core structure of Hurricane Erin diagnosed from high altitude dropsondes during CAMEX-4. *J. Atmos. Sci.*, **63**, 309–324, <https://doi.org/10.1175/JAS3596.1>.
- Helmus, J. J., and S. M. Collis, 2016: The Python ARM Radar Toolkit (Py-ART), a library for working with weather radar data in the Python programming language. *J. Open Res. Software*, **4**, e25, <https://doi.org/10.5334/jors.119>.
- Hirth, B. D., J. L. Schroeder, C. C. Weiss, D. Smith, and M. I. Biggerstaff, 2012: Research radar analyses of the internal

- boundary layer over Cape Canaveral, Florida, during the landfall of Hurricane Frances (2004). *Wea. Forecasting*, **27**, 1349–1372, <https://doi.org/10.1175/WAF-D-12-00014.1>.
- Hock, T. F., and J. L. Franklin, 1999: The NCAR GPS dropwindsonde. *Bull. Amer. Meteor. Soc.*, **80**, 407–420, [https://doi.org/10.1175/1520-0477\(1999\)080<0407:TNGD>2.0.CO;2](https://doi.org/10.1175/1520-0477(1999)080<0407:TNGD>2.0.CO;2).
- Houze, R. A., Jr., 2010: Clouds in tropical cyclones. *Mon. Wea. Rev.*, **138**, 293–344, <https://doi.org/10.1175/2009MWR2989.1>.
- Keper, J., 2001: The dynamics of boundary layer jets within the tropical cyclone core. Part I: Linear theory. *J. Atmos. Sci.*, **58**, 2469–2484, [https://doi.org/10.1175/1520-0469\(2001\)058<2469:TDOBLJ>2.0.CO;2](https://doi.org/10.1175/1520-0469(2001)058<2469:TDOBLJ>2.0.CO;2).
- , 2006: Observed boundary layer wind structure and balance in the hurricane core. Part II: Hurricane Mitch. *J. Atmos. Sci.*, **63**, 2194–2211, <https://doi.org/10.1175/JAS3746.1>.
- Knupp, K. R., J. Walters, and M. Biggerstaff, 2006: Doppler profiler and radar observations of boundary layer variability during the landfall of Tropical Storm Gabrielle. *J. Atmos. Sci.*, **63**, 234–251, <https://doi.org/10.1175/JAS3608.1>.
- Kosiba, K. A., and J. Wurman, 2014: Finescale dual-Doppler analysis of hurricane boundary layer structures in Hurricane Frances (2004) at landfall. *Mon. Wea. Rev.*, **142**, 1874–1891, <https://doi.org/10.1175/MWR-D-13-00178.1>.
- , —, F. J. Masters, and P. Robinson, 2013: Mapping of near-surface winds in Hurricane Rita using finescale radar, anemometer, and land-use data. *Mon. Wea. Rev.*, **141**, 4337–4349, <https://doi.org/10.1175/MWR-D-12-00350.1>.
- Krupar, R. J., J. L. Schroeder, D. A. Smith, S.-L. Kang, and S. Lorsolo, 2016: A comparison of ASOS near-surface winds and WSR-88D-derived wind speed profiles measured in landfalling tropical cyclones. *Wea. Forecasting*, **31**, 1343–1361, <https://doi.org/10.1175/WAF-D-15-0162.1>.
- Lorsolo, S., J. L. Schroeder, P. Dodge, and F. Marks, 2008: An observational study of hurricane boundary layer small-scale coherent structures. *Mon. Wea. Rev.*, **136**, 2871–2893, <https://doi.org/10.1175/2008MWR2273.1>.
- Ming, J., J. A. Zhang, R. F. Rogers, F. D. Marks, Y. Wang, and N. Cai, 2014: Multiplatform observations of boundary layer structure in the outer rainbands of landfalling typhoons. *J. Geophys. Res. Atmos.*, **119**, 7799–7814, <https://doi.org/10.1002/2014JD021637>.
- Montgomery, M. T., J. A. Zhang, and R. K. Smith, 2014: An analysis of the observed low-level structure of rapidly intensifying and mature Hurricane Earl (2010). *Quart. J. Roy. Meteor. Soc.*, **140**, 2132–2146, <https://doi.org/10.1002/qj.2283>.
- Morrison, I., S. Businger, F. Marks, P. Dodge, and J. A. Businger, 2005: An observational case for the prevalence of roll vortices in the hurricane boundary layer. *J. Atmos. Sci.*, **62**, 2662–2673, <https://doi.org/10.1175/JAS3508.1>.
- Naftel, J. C., 2009: NASA Global Hawk: A new tool for Earth science research. NASA Rep., 13 pp., <http://ntrs.nasa.gov/archive/nasa/casi.ntrs.nasa.gov/20090023138.pdf>.
- Nolan, D. S., J. A. Zhang, and D. P. Stern, 2009a: Evaluation of planetary boundary layer parameterizations in tropical cyclones by comparison of in situ observations and high-resolution simulations of Hurricane Isabel (2003). Part I: Initialization, maximum winds, and the outer-core boundary layer. *Mon. Wea. Rev.*, **137**, 3651–3674, <https://doi.org/10.1175/2009MWR2785.1>.
- , D. P. Stern, and J. A. Zhang, 2009b: Evaluation of planetary boundary layer parameterizations in tropical cyclones by comparison of in situ observations and high-resolution simulations of Hurricane Isabel (2003). Part II: Inner-core boundary layer and eyewall structure. *Mon. Wea. Rev.*, **137**, 3675–3698, <https://doi.org/10.1175/2009MWR2786.1>.
- Oye, R. C., C. Mueller, and S. Smith, 1995: Software for radar translation, visualization, editing, and interpolation. *27th Conf. on Radar Meteorology*, Vail, CO, Amer. Meteor. Soc., 359–361.
- Pazmany, A. L., J. B. Mead, H. B. Bluestein, J. C. Snyder, and J. B. Houser, 2013: A mobile rapid-scanning X-band polarimetric (RaXPo) Doppler radar system. *J. Atmos. Oceanic Technol.*, **30**, 1398–1413, <https://doi.org/10.1175/JTECH-D-12-00166.1>.
- Pilkey, J., and Coauthors, 2013: Rocket-and-wire triggered lightning in 2012 Tropical Storm Debby in the absence of natural lightning. *J. Geophys. Res. Atmos.*, **118**, 13 158–13 174, <https://doi.org/10.1002/2013JD020501>.
- Potvin, C. K., D. Betten, L. J. Wicker, K. L. Elmore, and M. I. Biggerstaff, 2012: 3DVAR versus traditional dual-Doppler wind retrievals of a simulated supercell thunderstorm. *Mon. Wea. Rev.*, **140**, 3487–3494, <https://doi.org/10.1175/MWR-D-12-00063.1>.
- Powell, M. D., P. J. Vickery, and T. A. Reinhold, 2003: Reduced drag coefficient for high wind speeds in tropical cyclones. *Nature*, **422**, 279–283, <https://doi.org/10.1038/nature01481>.
- Ren, Y., J. A. Zhang, S. R. Guimond, and X. Wang, 2019: Hurricane boundary layer height relative to storm motion from GPS dropsonde composites. *Atmosphere*, **10**, 339, <https://doi.org/10.3390/atmos10060339>.
- Rogers, R. F., and Coauthors, 2017: Rewriting the tropical record books: The extraordinary intensification of Hurricane Patricia (2015). *Bull. Amer. Meteor. Soc.*, **98**, 2091–2112, <https://doi.org/10.1175/BAMS-D-16-0039.1>.
- Savelyev, S. A., and P. A. Taylor, 2005: Internal boundary layers: I. Height formulae for neutral and diabatic flows. *Bound.-Layer Meteor.*, **115**, 1–25, <https://doi.org/10.1007/s10546-004-2122-z>.
- Schroeder, J., B. Edwards, and I. Giammanco, 2009: Observed tropical cyclone wind flow characteristics. *Wind Struct.*, **12**, 349–381, <https://doi.org/10.12989/was.2009.12.4.349>.
- Sibson, R., 1981: A brief description of natural neighbor interpolation. *Interpreting Multivariate Data*, Wiley, 21–36.
- Stern, D. P., G. H. Bryan, and S. D. Aberson, 2016: Extreme low-level updrafts and wind speeds measured by dropsondes in tropical cyclones. *Mon. Wea. Rev.*, **144**, 2177–2204, <https://doi.org/10.1175/MWR-D-15-0313.1>.
- Tang, X., and Z. Tan, 2006: Boundary-layer wind structure in a landfalling tropical cyclone. *Adv. Atmos. Sci.*, **23**, 737–749, <https://doi.org/10.1007/s00376-006-0737-3>.
- Torres, S. M., Y. F. Dubel, and D. S. Zrnić, 2004: Design, implementation, and demonstration of a staggered PRT algorithm for the WSR-88D. *J. Atmos. Oceanic Technol.*, **21**, 1389–1399, [https://doi.org/10.1175/1520-0426\(2004\)021<1389:DIADOA>2.0.CO;2](https://doi.org/10.1175/1520-0426(2004)021<1389:DIADOA>2.0.CO;2).
- UCAR/NCAR, 2005: NSF/NCAR GV HIAPER aircraft. Earth Observing Laboratory, <http://doi.org/10.5065/D6DR2SJP>.
- Uhlhorn, E. W., and P. G. Black, 2003: Verification of remotely sensed sea surface winds in hurricanes. *J. Atmos. Oceanic Technol.*, **20**, 99–116, [https://doi.org/10.1175/1520-0426\(2003\)020<0099:VORSSS>2.0.CO;2](https://doi.org/10.1175/1520-0426(2003)020<0099:VORSSS>2.0.CO;2).
- Vickery, P. J., D. Wadhera, M. D. Powell, and Y. Chen, 2009: A hurricane boundary layer and wind field model for use in engineering applications. *J. Appl. Meteor. Climatol.*, **48**, 381–405, <https://doi.org/10.1175/2008JAMC1841.1>.
- Williams, G. J., 2019: Idealized simulations of the inner core boundary layer structure in a landfalling tropical cyclone. Part

- I: Kinematic structure. *Trop. Cyclone Res. Rev.*, **8**, 47–67, <https://doi.org/10.1016/j.tcr.2019.07.006>.
- Willoughby, H. E., and M. B. Chelmon, 1982: Objective determination of hurricane tracks from aircraft observations. *Mon. Wea. Rev.*, **110**, 1298–1305, [https://doi.org/10.1175/1520-0493\(1982\)110<1298:ODOHTF>2.0.CO;2](https://doi.org/10.1175/1520-0493(1982)110<1298:ODOHTF>2.0.CO;2).
- Wurman, J., and J. Winslow, 1998: Intense sub-kilometer-scale boundary layer rolls observed in Hurricane Fran. *Science*, **280**, 555–557, <https://doi.org/10.1126/science.280.5363.555>.
- Zhang, J. A., K. B. Katsaros, P. G. Black, S. Lehner, J. R. French, and W. M. Drennan, 2008: Effects of roll vortices on turbulent fluxes in the hurricane boundary layer. *Bound.-Layer Meteor.*, **128**, 173–189, <https://doi.org/10.1007/s10546-008-9281-2>.
- , R. F. Rogers, D. S. Nolan, and F. D. Marks, 2011: On the characteristic height scales of the hurricane boundary layer. *Mon. Wea. Rev.*, **139**, 2523–2535, <https://doi.org/10.1175/MWR-D-10-05017.1>.
- , —, P. D. Reasor, E. W. Uhlhorn, and F. D. Marks, 2013: Asymmetric hurricane boundary layer structure from dropsonde composites in relation to the environmental vertical wind shear. *Mon. Wea. Rev.*, **141**, 3968–3984, <https://doi.org/10.1175/MWR-D-12-00335.1>.